Key Points:
- We find no clear evidence of water at most of the previously proposed lake sites
- Locations, where altimetry detected active lakes, do not exhibit lake characteristics in RES
- Lakes far upstream the main trunk are not triggering enhanced ice flow

Correspondence to:
A. Humbert,
angelika.humbert@awi.de

Missing Evidence of Widespread Subglacial Lakes at Recovery Glacier, Antarctica

Angelika Humbert[1,2] (ID), **Daniel Steinhage**[1] (ID), **Veit Helm**[1] (ID), **Sebastian Beyer**[1,3] (ID), and **Thomas Kleiner**[1] (ID)

[1] Alfred Wegener Institute Helmholtz Centre for Polar and Marine Research, Bremerhaven, Germany, [2] Department of Geosciences, University of Bremen, Bremen, Germany, [3] Potsdam Institute for Climate Impact Research, Potsdam, Germany

Abstract Recovery Glacier reaches far into the East Antarctic Ice Sheet. Recent projections point out that its dynamic behavior has a considerable impact on future Antarctic ice loss (Golledge et al., 2017, https://doi.org/10.1002/2016GL072422). Subglacial lakes are thought to play a major role in the initiation of the rapid ice flow (Bell et al., 2007, https://doi.org/10.1038/nature05554). Satellite altimetry observations have even suggested several actively filling and draining subglacial lakes beneath the main trunk (B. E. Smith et al., 2009, https://doi.org/10.3189/002214309789470879). We present new data of the geometry of this glacier and investigate its basal properties employing radio-echo sounding. Using ice sheet modeling, we were able to constrain estimates of radar absorption in the ice, but uncertainties remain large. The magnitude of the basal reflection coefficient is thus still poorly known. However, its spatial variability, in conjunction with additional indicators, can be used to infer the presence of subglacial water. We find no clear evidence of water at most of the previously proposed lake sites. Especially, locations, where altimetry detected active lakes, do not exhibit lake characteristics in radio-echo sounding. We argue that lakes far upstream the main trunk are not triggering enhanced ice flow, which is also supported by modeled subglacial hydrology.

1. Introduction

Recovery Glacier drains an area of ~996,000 km^2, corresponding to ~8 % of the area and ~5% of the volume of the East Antarctic Ice Sheet (EAIS; Rignot et al., 2008). It was first explored in 1957 by the Commonwealth Transantarctic Expedition (Lister & Pratt, 1959). The drainage basin is traversed by the main ice stream, Recovery Glacier, flanked to its north by the Shackleton Mountain Range and fed by several tributary glaciers including Ramp and Blackwall. Its drainage basin ranges nearly 1,000 km from the interior EAIS to Filchner Ice Shelf (Figure 1). Golledge et al. (2017) demonstrated that the majority of the future mass loss from the EAIS will originate from the Recovery basin, underlining the importance of understanding its dynamics and, in turn, the role subglacial water plays in influencing them. Previous studies based on surface structure, elevation change, and radio-echo sounding (RES) argue that prominent subglacial lakes exist beneath Recovery Glacier (Bell et al., 2007; Fricker et al., 2014; Smith et al., 2009). These lakes have been implicated in both the ice stream's onset and its fast flow, although there remains a poor understanding of the processes by which subglacial lakes overall influence ice dynamics in Antarctica (Ashmore et al., 2014; Siegert et al., 2014). Apart from lakes, basal water may occur either in the form of a distributed layer — like a thin film — or as a network of channels, which both affect sliding.

Observations at the ice base are limited by accessibility, which usually restricts analysis to indirect methods. However, significant differences in the dielectric properties of subglacial water and rock (or sediment) result in different reflection coefficients of radar waves, which can be analyzed in order to detect water at the reflection interface (and infer the base of the ice is wet). However, it requires a reasonable estimate of the absorption in the ice, which depends on the (unknown) temperature distribution in the ice. For this reason previous studies used the spatial variability of the reflection loss in combination with the hydraulic head (e.g., Langley et al., 2014) or basal roughness (e.g., Diez et al., 2018), instead of the absolute magnitude, to estimate basal conditions.

Repeat satellite altimetry missions, for example, ICESat, provided comprehensive topography data sets of Antarctica, which allowed to detect changes in surfaces topography on rather sort time scales. Many of these
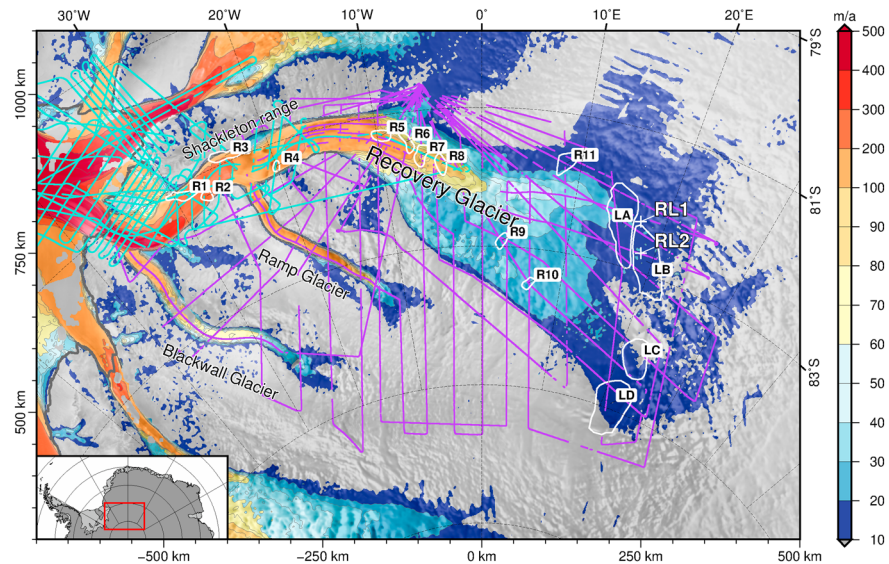
Figure 1. Map of the Recovery basin area with selected place names. Lakes observed by Bell et al. (2007) marked with LA–LD and Smith et al. (2009) marked with R1–R11, both outlined in white. Dots indicate basal returns of the radio-echo signal from this study (purple) and from Operation IceBridge (Leuschen et al., 2010, updated 2017), turquoise. Surface velocities (blue to red) derived from satellite radar interferometry (Rignot et al., 2011) are clipped at the 10 m/year lower limit. The thick gray line denotes the grounding line position. In this and all subsequent maps the background image is Ramp Antarctic Mapping Mission 1 mosaic (Jezek, 1999), whereas delineations for ice extend and grounding line position are from the SCAR Antarctic Digital Database, version 4 (British Antarctic Survey, 2004).

changes were attributed to subglacial lakes (Smith et al., 2009). In recent years, the method of the detection of active lakes by means of altimetry has been challenged by findings of Siegert et al. (2014), who found no evidence for an active lake site in the Institute Ice Stream in RES data. Wright et al. (2014) came to the same conclusion for 11 sites at Byrd Glacier catchment. Siegert et al. (2016) demonstrated the capability and limits of radar and remote sensing methods to locate subglacial lakes and infer its dynamics, which also challenged the current view on active lakes. Our study pursues this path of critical evaluation of various methods by its application on a new data set of airborne RES data. In January 2014 an extensive airborne survey of Recovery Glacier and its drainage basin was carried out, surveying a total length of 22,700 km. Ice thickness, ice structure, and surface topography data were acquired, extending the region mapped by earlier surveys (Diez et al., 2018; Forsberg et al., 2018; Paxman et al., 2017) further southeast. Our survey aimed to accomplish two goals: (1) acquire extensive basic coverage of Recovery Glacier and its tributaries, Ramp Glacier, and Blackwall Glacier (see Figure 1) and (2) collect data along flow lines of the main trunk and detailed coverage of the proposed lake areas. A surface velocity data set derived by Floricioiu et al. (2014) was used to compute flow lines prior to the survey. The resulting profiles are shown in Figure 1 together with the previously proposed lakes by Bell et al. (2007) and Smith et al. (2009) (referred to as LA–LD and Lakes R1–R11, respectively, in the following).

We examine the magnitude of the basal reflection coefficient and its determining factors and discuss the general ability and limits of this approach. The basal reflection coefficient in conjunction with additional parameters, such as modeling of subglacial hydrology, mapping surface elevation change, reflectivity, and variability of reflection loss, is used to review previously proposed lake locations.

2. Methods

The following sections summarize the modeling studies we conducted to study the subglacial properties of Recovery Glacier and its tributaries. We introduce the deployed RES system and present methods applied to obtain bed elevation and the approach to distinguish between wet or dry bed returns. Furthermore, the method used to determine active lakes based on ICESat altimetry is described.

2.1. Subglacial Lake Identification From Modeling
Two different modeling studies were conducted to derive englacial and basal thermal conditions as well as subglacial water fluxes and sinks with emphasis on the Recovery Glacier region.

Table 1
Summary of the Data Sets Applied as Boundary Conditions for the Different PISM Simulations, Where T_s Is the Ice Surface Temperature, a_s Is the SMB, and q_{geo} Is the Geothermal Flux

Forcing	Reference	Value
T_s^{RA}	van Wessem et al. (2014)	(-42 ± 7) °C
T_s^{FaO}	Fortuin and Oerlemans (1990)	(-39 ± 9) °C
T_s^{JCo}	Comiso (2000)	(-36 ± 9) °C
a_s^{RA}	van Wessem et al. (2014)	$(19 \pm 9)\ 10^{-7}$ (kg/m^2 s)
a_s^{VB}	van de Berg et al. (2006)	$(19 \pm 7)\ 10^{-7}$ (kg/m^2 s)
a_s^{Ar}	Arthern et al. (2006)	$(24 \pm 12)\ 10^{-7}$ (kg/m^2 s)
q_{geo}^{P}	Purucker (2012)	$(42 \pm 8)\ 10^{-3}$ W/m^2
q_{geo}^{S}	Shapiro and Ritzwoller (2004)	$(48 \pm 4)\ 10^{-3}$ W/m^2
q_{geo}^{F}	Fox Maule et al. (2005)	$(59 \pm 8)\ 10^{-3}$ W/m^2

Note. Spatial means and standard deviations were evaluated on the initial 1-km grid for Recovery area only. The original data set of Fox Maule et al. (2005) was capped at a value of 0.07 W/m^2 according to the recommendation for the SeaRISE-Antarctica setup (Bindschadler et al., 2013). PISM = Parallel Ice Sheet Model; SMB = Surface Mass Balance.

2.1.1. Englacial and Subglacial Temperature Fields

We engaged numerical ice flow modeling to derive a first-order estimate of the basal thermal regime across Antarctica, similar to previous studies (e.g., Ashmore et al., 2014; Matsuoka et al., 2012; Wright et al., 2012). The simulated temperature-depth profiles at each grid location were also used to derive englacial attenuation in support of our RES analyses introduced in section 2.2.

Here we used the Parallel Ice Sheet Model (PISM v0.6.2, Bueler & Brown, 2009; Winkelmann et al., 2011). PISM solves the nonsliding shallow ice approximation (SIA) and the shallow shelf approximation (SSA) for grounded ice, where the SSA solution acts as a sliding law, and only the SSA for floating ice. New ice thickness data derived for this study (methods described in section 2.2.2 were used for different simulations with varying data sets for boundary conditions as follows: surface temperature (Comiso, 2000; Fortuin & Oerlemans, 1990; van Wessem et al., 2014), surface mass balance (Arthern et al., 2006; van de Berg et al., 2006; van Wessem et al., 2014), geothermal flux (Fox Maule et al., 2005; Shapiro & Ritzwoller, 2004)), and the update from Purucker (2012) based on the method of Fox Maule et al. (2005). The original data set of Fox Maule et al. (2005) was capped at a value of 0.07 W/m^2 according to the recommendation for the SeaRISE-Antarctica setup (Bindschadler et al., 2013). A summary of the selected data sets is given in Table 1.

The ice sheet models used in Matsuoka et al. (2012) and Ashmore et al. (2014) are based on a balance velocities approach, where the vertical distribution of velocity is calculated based on shape functions (Leysinger Vieli et al., 2011; Pattyn, 2010). This is in contrast to PISM, where the vertical velocity within the ice is given by the incompressibility. Another major difference of our model setup to the flow model applied in Wright et al. (2012) is that the geothermal heat flux in our study is not spatially invariant.

In a series of successive grid refinements (all based on the initial 1 km present-day geometry) using 40, 20, and 10 km horizontal resolution and 41, 81, and 101 vertical layers, respectively, a present-day state of the Antarctic Ice Sheet was computed for each combination of boundary conditions, with the restriction that RACMO2.3/ANT (van Wessem et al., 2014) data for mean annual skin temperature and accumulation rate were used in conjunction for consistency. Thus, a combination of five different surface forcings for three different geothermal fluxes was used to build the ensemble.

In one group of simulations, we applied PISM's flux correction method, where the climatic mass balance was modified at each time step to obtain an ice sheet thickness in closer agreement with measurements (hereinafter referred to as evoFT). In this group, we further prescribed the present-day calving front position according to Bedmap2 (Fretwell et al., 2013). In the second group of simulations, the ice thickness and calving front position were allowed to evolve freely (hereinafter referred to as evoSR). In all simulations, we applied the subgrid grounding line interpolation scheme (Feldmann et al., 2014) for a better grounding line

representation in the relatively coarse model, while other parameters correspond to PISM's SeaRISE-Antarctica setup (cf. the Potsdam model in Nowicki et al., 2013). After initialization (1 year), a short relaxation period (100 years), and a purely thermal spin-up with the geometry held fixed (200 ka) on the 40 km grid using only the nonsliding SIA, the model ran for 100, 20, and 4 ka on the 40, 20, and 10 km grid, respectively, in the hybrid (SIA + SSA) mode for each setup to reach the final temperature distribution used here.

The results of all model runs were analyzed for the temperate ice area fraction (TIAF), as a temperate base is a prerequisite for subglacial water. TIAF was calculated as the ratio between the grounded temperate ice area and total grounded ice area. In addition, we computed the temperate ice volume fraction (TIVF) as the ratio between temperate ice volume and the total grounded ice volume. With the TIVF we have measured the amount of very warm ice (at pressure melting point) near the base that contributes to the attenuation of the radar signal.

2.1.2. Subglacial Water Flux and Hydraulic Potential

The new ice geometry (ice thickness, H, and ice base, h_b) together with the basal melt rates from ice modeling was used to estimate the water flux. Subglacial water flux and storage are governed by the hydraulic potential Φ, which depends on the elevation potential and the water pressure p_w (Shreve, 1972)

$$\Phi = \rho_w g h_b + p_w, \tag{1}$$

with the acceleration due to gravity g and density of water $\rho_w = 1{,}000$ kg/m^3. The water pressure depends on the ice overburden pressure and the effective pressure N (normal stress at the bed minus water pressure)

$$p_w = \rho_i g H - N, \tag{2}$$

wherein $\rho_i = 910$ kg/m^3 is the density of ice. Following previous authors such as Le Brocq et al. (2009) and Livingstone et al. (2013), we assumed the water flows as a thin (a few millimeters) and distributed water film. Under this premise, the water pressure and the ice overburden pressure are in equilibrium, and therefore, the effective pressure is zero. This enabled us to reformulate equation (1) as

$$\Phi = \rho_w g h_b + \rho_i g H, \tag{3}$$

to derive the water flux with a simple flux routing scheme as described by Le Brocq et al. (2006). This approach is only valid at large (km) scales and is not able to include local features such as channels. Also, lakes that are formed by ice dynamic mechanisms are not captured by this.

We interpolated the melt rates given by the PISM model onto a 1-km grid. The hydraulic potential was computed following equation (1) before smoothing it with a 10-km radius box blur filter. This was done to make use of our high-resolution ice surface while accounting for the averaged sheet flow assumption. Additionally, a version of the potential with 2-km smoothing filter was generated as a basis for the identification of lake candidates from additional criteria (see section 2.4). Then local sinks in the hydraulic potential were marked as expected positions for subglacial lakes. The flux routing method requires that every cell has a defined flow direction and that by successively following these directions, the boundary of the study area is reached. Therefore, local sinks and flat areas must be removed prior to applying the routing scheme. We accomplished this by using a Priority-Flood algorithm as described in Barnes et al. (2014b), which fills depressions in a single pass and then adds a small gradient to the resulting flats. The gradient generation toward the outlet of the depression ensures that the hydraulic potential is altered in the smallest possible way (see Barnes et al., 2014a, for details). This procedure is a very efficient way to guarantee that all water is drained into the ocean.

We calculated the hydraulic potential and resulting water flux for different melt rate distributions: catchment-wide melting of 0.006 m/year and melt rates from the evoSR type simulations using q_{geo}^S, q_{geo}^P, and q_{geo}^F. This allowed us to differentiate between flow paths that were theoretically possible and those that were likely developed with the available water.

Note that we only routed the water that was produced within the investigated area and not the entire Recovery drainage basin, since we were only interested in the general distribution pattern rather than the magnitude of the flux.

2.2. Ice Thickness From RES

2.2.1. Survey and AWI-RES System

To map the ice thickness and basal properties of the Recovery basin, we undertook an extensive RES survey in January 2014. The flight tracks, totalling 22,700 km in length and depicted in Figure 1, were designed

to achieve a basic coverage across the Recovery catchment, while additionally targeting flow lines along Recovery Glacier and its tributary glaciers including Ramp and Blackwall and more detailed coverage across the proposed subglacial lakes from Bell et al. (2007) and Smith et al. (2009). Flow lines were derived from Floricioiu et al. (2014).

We surveyed with the Alfred Wegener Institute RES system (hereafter AWI-RES), operating at a carrier frequency of 150 MHz. Building upon the basic design reported by Nixdorf et al. (1999), the system deployed in 2014 used a new signal generator inside the transmitter and a completely revised receiver. The transmitted signals were generated by a programmable digital synthesizer which started each burst with the same phase. The new receiver was based on a 14-bit digitizer with 4 ns sampling interval but retained the concept of different preamplifying and logarithmic detectors (Nixdorf et al., 1999). This system has a large dynamic range of −105 to +10 dBm. The antenna hardware and signal handling between transmitter, receiver, and antennas remained unchanged from that reported by Nixdorf et al. (1999).

The system was operated in mono burst mode, transmitting a long noncoherent pulse of $\tau = 600$ ns. The received power was rectified, and the envelope was recorded. Subsequently, shots were incoherently stacked 1,024 fold for improving signal-to-noise ratio and then recorded at a rate of 15 Hz. The corresponding average shot separation was 6 m. The accuracy of the travel time measurements was determined by the sample interval of 4 ns, corresponds to 0.34 m in ice. The recording time window was 64 μs, allowing registration of reflections up to a maximum ice thickness of 5,000 m, on a flight level of 600 m above ground. Processing of the data before evaluation comprised further stacking of shots (sevenfold) and filtering. From this point on, two processing branches were followed: first, scaled amplitudes were used to pick the basal reflections in order to estimate ice thickness and second, unscaled amplitudes were used to analyze the basal reflectivity.

The AWI-RES system differs in some parameters from the systems deployed by other groups. The small bandwidth of 1,666 kHz ($= \tau^{-1}$) results in a vertical resolution of approximately 50 m and a radius of the first Fresnel zone of ~300 m (assuming 3,000 m thick ice and a flight level of 600 m above ground). Radar waves are diffusively scattered at small facets (small with respect to wavelength) within the first Fresnel zone. The width and intensity of the bedrock return are controlled by the number and size distribution of the corresponding scattering elements. For large Fresnel zones usually enough scattering elements are available to form intensity peaks with a similar width. However, the peak intensity will change from trace to trace by several decibels, which is known as the radar speckle. Incoherent stacking along track reduces this speckle effect slightly. In consequence, the AWI-RES system with its long pulse duration is sensitive neither to small-scale changes in bed roughness nor to specular surfaces, which has implications for our ability to detect subglacial lakes that we discuss in detail below.

2.2.2. Ice Thickness and Subglacial Topography

To improve and densify the manual picked ice thickness retrievals as well as to evaluate the return power, an automatic algorithm determining the basal reflection in a predefined time window on a shot to shot basis was developed. The algorithm generated a quality flag for each pick, based on the noise floor before and after the bed pick and, where the reported quality was low, we undertook manual picking. The resulting two-way travel times in ice were converted into thickness by using locally determined velocity depth functions. The appropriate velocities were calculated by computing depth density profiles (Herron & Langway, 1980) using accumulation and temperature distribution of the regional atmospheric climate model RACMO2.3 (van Wessem et al., 2014).

For the interpolation of direct ice thickness measurements onto an ice thickness grid, we first selected a polygon surrounding the data with a margin of approximately 50 km including only the grounded ice area. Within that polygon, we further incorporated Operation IceBridge data from the years 2011/2012 and 2012/2013 (Leuschen et al., 2010, updated 2017) and the locations of known rock outcrops from ADD4 (British Antarctic Survey, 2004). In addition to these point observations, gridded data from Bedmap2 (Fretwell et al., 2013) were used outside the polygon toward the domain margin (see Figure 1 for domain extent). The ice thickness data have been interpolated on an initial 5-km × 5-km grid using the continuous curvature splines in tension algorithm (Smith & Wessel, 1990) and resampled to the final 1 km resolution grid. After interpolation, the data inside the polygon were stenciled out of the regional grid and incorporated into the Bedmap2 ice thickness grid. We further subtracted this subset of the regional ice thickness grid from the Bedmap2 surface topography to incorporate the new basal topography into the Bedmap2 bedrock grid. Bedmap2 surface topography was used to be consistent with the Bedmap2 bedrock topography.

2.3. Basal Reflection Coefficient

Previous studies have suggested that where englacial attenuation can be accounted for, the strength of the returned radar echo from the ice bed interface, here termed the basal reflection coefficient, can be used as a proxy for the thermal condition of the ice bed (Ashmore et al., 2014; Diez et al., 2018; Gades et al., 2000; Jacobel et al., 2010; Langley et al., 2011; Rippin et al., 2006). We follow this principle by rearranging the radar equation (Bogorodsky et al., 1985) for the reflection loss ($L_R = |r|^{-2}$), where P_r denotes the power of the received RES signals, P_t the transmitted power, H the ice thickness, h the height of the aircraft above ground, G the antenna gain, q the refraction gain, λ the wavelength of the RES carrier frequency, L_K the cable losses of the RES system, L_T the transmission loss at the surface of the ice, and L_A absorption in the ice; it is possible to calculate the basal reflection coefficient

$$L_R = \frac{P_t G^2 q \lambda^2}{(4\pi)^2 [2(H+h)]^2 L_K^2 L_T^2 L_A P_r} = \frac{C_1}{P_r} \frac{1}{L_A} = \frac{1}{r^2}. \tag{4}$$

Except for L_A and L_R, all parameters are measured for each shot or are constants of the system and can be represented as a single constant C_1. Thus, if L_A can be determined, it is possible to calculate basal reflection loss. However, if L_A is overestimated, r becomes > 1, a nonphysical value.

The received signal power P_r was obtained by selecting the maximum amplitude within a time window for each shot ranging -300 to $+900$ ns from the manually picked, as well as automatically detected, basal reflector, accounting for picking errors. In order to evaluate the maximum amplitude representing a basal reflector, we compared the standard deviation of the amplitudes to the maximum amplitude found within this time window. Oswald and Gogineni (2008) suggested the integrated power (P_r^{ig}) across the whole bed return to minimize the radar speckle within the Fresnel zone. Thus, we integrated P_r across ± 800 ns of the bed peak position, a slightly larger and symmetrical zone around the bed peak position, for each shot to derive P_r^{ig}.

For each bed reflection L_R^{ig} was estimated using equation (4). Finally, we derived the full width half maximum of the frequency distribution of L_R^{ig} within a moving window of 2,500 shots (~ 105 km). By correcting the returned power for geometric effects and using an average attenuation rate, the presence of only two different basal regimes — wet and dry — should result in a bimodal distribution in the histogram of the corrected return power (Oswald & Gogineni, 2008). However, this approach required that a significant portion of both classes were covered by the profile under examination.

In our analysis we used unstacked and stacked (along track) amplitudes as well as stacked integrated power, respectively. As previous studies (e.g., Langley et al., 2011) have estimated the nature of the bed from assessing variability in $[P_r]_{dB} - [C_1]_{dB} + [L_A]_{dB}$, we also computed this quantity.

The total attenuation L_A integrated over the two-way travel path between the surface h_s and the base h_b can be written as (Matsuoka et al., 2010) follows:

$$[L_A]_{dB} = 2 \left[\int_{h_b}^{h_s} A(z)\, dz \right]_{dB}, \tag{5}$$

where $A(z)$ is the local attenuation rate per unit path length (one way) in vertical (z) direction. The local attenuation rate A (unit: dB/m) in ice depends on the permittivity $\varepsilon' = 3.2$ and the conductivity σ of the ice. The permittivity is assumed to be constant (cf. MacGregor et al., 2007), while the conductivity varies with depth in the local ice column; thus (Matsuoka et al., 2012; Zirizzotti et al., 2010),

$$[A(z)]_{dB} = 8.686 \sqrt{\frac{\mu_0}{\varepsilon_0 \varepsilon'}} \frac{\sigma(z)}{2} = 914.63\, \sigma(z), \tag{6}$$

where $\varepsilon_0 = 8.8541878176 \times 10^{-12}$ F/m^{-1} and $\mu_0 = 1.25663706 \times 10^{-6}$ N/A^2 are the free space dielectric permittivity and magnetic permeability. The conductivity $\sigma(z)$ depends on temperature following an Arrhenius model

$$\sigma(z) = \sigma_0 \exp\left[\frac{E}{k} \left(\frac{1}{T_r} - \frac{1}{T(z)} \right) \right], \tag{7}$$

where $E = 0.51$ eV is the activation energy, $k = 8.6173324 \times 10^{-5}$ eV/K is the Boltzmann constant, and σ_0 being a reference conductivity for pure ice. In general, the effect of impurities can be parameterized. However,

as $\sigma(z)$ is dominated by the effect of temperature, in a study area of limited extent, we neglect the effect of impurities and use $\sigma_0 = 9.2$ μS/m for pure ice conductivity at $T_r = 251$ K (Matsuoka et al., 2012).

Thus, the two-way attenuation could be calculated once the local temperature distribution in the ice is known. We derived the required temperature fields from the modeling introduced in section 2.1.1. With this, we estimated r and used this as one criterion for assessing the nature of the bed.

2.4. Subglacial Lake Identification

In our lake identification scheme, we followed the procedure of Carter et al., (2007, Carter scheme) and began to identify lake candidates from the hydrology, which was required to define an area over which quantities that we used to assess the characteristics of the potential lakes were averaged. For this purpose we estimated the hydraulic potential in the along-track direction (1-D), as well as used sinks in the hydraulic potential (2-D, description of the hydraulic model follows below). For the 1-D case, we strictly followed Carter et al. (2007). For the 2-D approach, we smoothed the potential with a box blur filter (2 km radius). Across these lake candidates, we engaged two criteria for assessing the existence of a lake based on RES.

1. Basal reflectivity criterion: $\overline{PPC}_{lake} > 0.95$, where $\overline{PPC}_{lake}$ is defined as the mean of all values across the lake candidate.
2. Relative power criterion: $\bar{L}_{R_{lake}} > \bar{L}_{R_{surr}} + 5$ dB. $\bar{L}_{R_{lake}}$ is defined as the mean of all L_R values across the lake candidate and $\bar{L}_{R_{surr}}$ as the mean of all L_R values in the area before and after the lake candidate. By definition those areas have the same extent as the lake candidate but are not larger than 20 km and not smaller than 3 km.

As discussed above, our RES system was not sensitive to specular surfaces. Therefore, we were unable to use the specularity, defined as the normalized standard deviation of the echo power of all shots within 200 m of a shot (Carter et al., 2007), for assessing the existence of lakes. A typical bed peak of AWI-RES had a skewed Gaussian shape with a half beam width of 300 ns. Instead of specularity we used the peak-to-peak correlation (PPC) to estimate the similarity of bed reflections within the first Fresnel zone. If a thick water body was present, the roughness should have been small, and all bed peaks should have been very similar in amplitude and shape, resulting in high PPC. In cases with strong radar speckle (thin water layers) or prominent small-scale roughness, the bed peaks should have varied within the Fresnel zone resulting in lower PPC. PPC was calculated in a running window along track for each autodetected bed peak as follows:

$$PPC(i) = \frac{1}{n} \sum_{j=i-n/2}^{j=i+n/2} C_i C_j,$$ (8)

where $C_i C_j$ is the cross correlation of two bed peaks centered at its maximum spreading of 1,600 ns (twice the pulse length with 200 ns margin at both ends). The number of bed peaks n was chosen to cover the Fresnel zone of approximately 300 m and contains at least 20% automatically detected bed peaks of all shots within the Fresnel zone.

2.5. Active Lake Identification From Satellite Altimetry

In addition to our airborne survey we also drew on ICESat altimetry data to identify locations of potentially active lakes. To identify outlines of active lakes within our research area, we slightly modified the along-track processing approach presented by Smith et al. (2009) and Fricker et al. (2014) using ICESat data release 34. We mapped the ICESat tracks of the 17 laser campaigns acquired between 2003 and 2009 to a reference orbit. Since the tracks are offset to the reference orbit by up to 400 m, it is necessary to account for topography and/or cross-track slope errors. Our approach is slightly different to the improved repeat track technique introduced by Fricker et al. (2014) but gave very similar results. Instead of estimating linear trends in subswaths to correct for across-track slope, we used a reference DEM of Helm et al. (2014) to derive the topographic correction. In both cases all ICESat tracks of the different campaigns were projected to the reference orbit to be able to estimate elevation change.

To determine active lakes, a mean elevation profile along the reference orbit track was derived. For each of the 250 m along-track positions we averaged all topographically corrected data within 1 km distance. Subsequently, the elevation difference to the mean elevation profile for each of the 17 laser campaigns was calculated, producing similar Gaussian-shaped elevation anomalies over active lakes as previously presented by Smith et al. (2009) and Fricker et al. (2014). In a final step we separately integrated all positive and negative
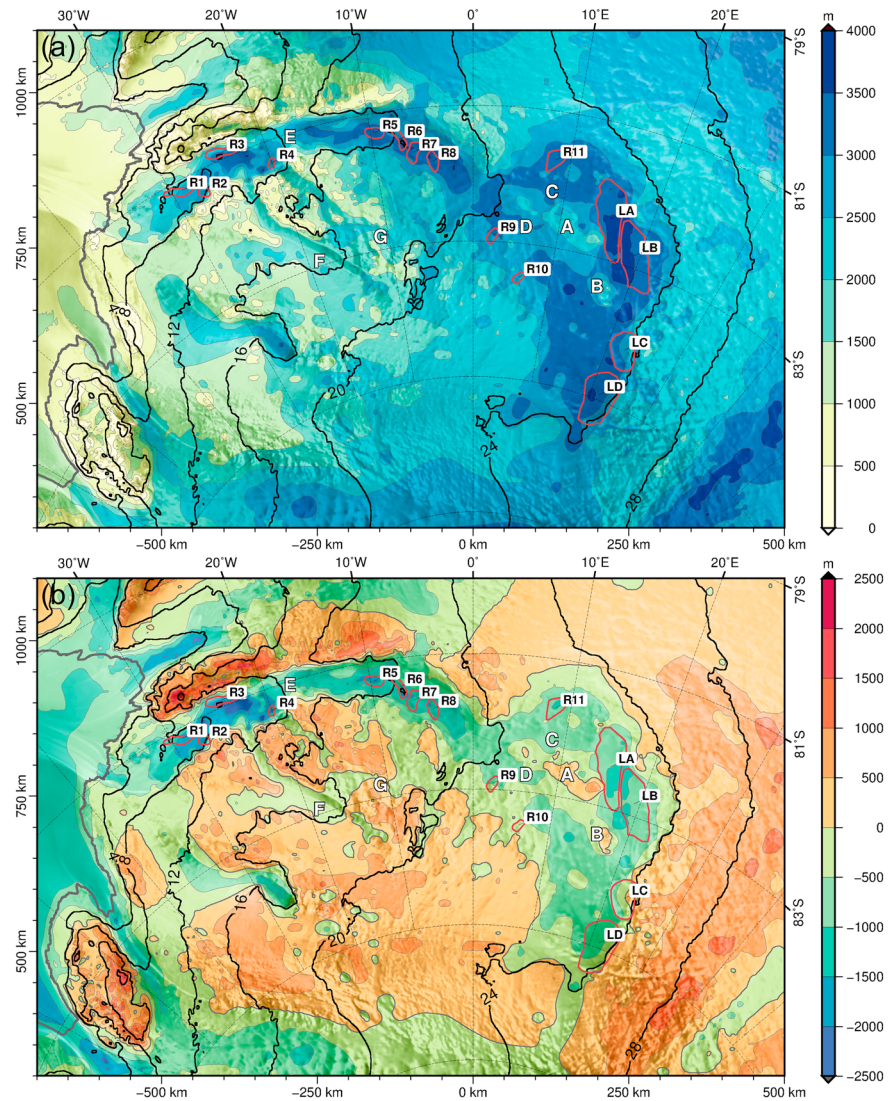
Figure 2. New ice thickness data generated using the methods outlined in sections 2.2.1 and 2.2.2 (a) and basal topography based on the ice thickness grid shown in (a) and Bedmap2 surface topography (Fretwell et al., 2013) (b). Superimposed are previously proposed lake outlines (Bell et al., 2007; Smith et al., 2009) in red and contours of the hydraulic potential annotated every 4 MPa. Feature names A–G are used in the main text. The thick gray line denotes the present-day grounding line position.

anomalies along the reference orbits and interpolated the data to two grids with a 1 km pixel spacing using inverse distance weighting within a 5 km search radius.

3. Results

3.1. Ice Thickness and Subglacial Topography

Figure 1 shows all points where ice thickness data were obtained. Along the main trunk of Recovery Glacier, just upstream from the junction with Ramp Glacier, almost no basal reflections could be obtained, neither along nor across flow direction. No reflections were recovered east of LB, across LC, or across the southern extent of LD. Elsewhere, the coverage was good, with basal reflections achieved for 74% of RES profiles. The new ice thickness and subglacial topography DEMs are shown in Figure 2.

The thinnest ice drapes across the Shackleton Range (Figure 2), marking the northwestern boundary of Recovery Glacier's main trunk. Transecting the Shackleton Range at approximately S81°, W005° is a region of thicker ice, ~2,500 m deep, beneath which the subglacial reflector at <1,000 m elevation is very smooth. This bears the characteristics of an ice stream tributary but which is currently shut down according to surface ice

Table 2
Thermal Properties Derived From the Different PISM Simulations, Where the TIAF and the TIVF Are Given in Percent

	Forcing	q_{geo}^P		q_{geo}^S		q_{geo}^F	
		TIAF	TIVF	TIAF	TIVF	TIAF	TIVF
evoFT	T_s^{RA}, a_s^{RA}	**17.6**	**0.47**	50.7	0.61	71.9	0.69
	T_s^{FaO}, a_s^{Ar}	19.6	0.55	46.5	0.70	75.1	0.80
	T_s^{FaO}, a_s^{VB}	19.3	0.55	45.4	0.70	74.9	0.78
	T_s^{JCo}, a_s^{Ar}	28.8	0.72	62.9	0.88	**85.3**	**0.98**
	T_s^{JCo}, a_s^{VB}	28.6	0.72	62.9	0.87	85.1	0.96
evoSR	T_s^{RA}, a_s^{RA}	**24.7**	**0.71**	60.6	0.77	83.0	0.84
	T_s^{FaO}, a_s^{Ar}	32.1	1.04	64.4	1.10	82.3	1.09
	T_s^{FaO}, a_s^{VB}	31.4	1.03	64.0	1.08	82.4	**1.13**
	T_s^{JCo}, a_s^{Ar}	33.8	0.92	73.6	1.00	**88.7**	1.00
	T_s^{JCo}, a_s^{VB}	31.4	0.88	72.4	0.95	87.4	0.95

Note. Bold numbers are high lighting minimum and maximum values of the evoFT and evoSR runs. All quantities are calculated for the grounded part of Recovery Glacier area on PISM's final 10-km resolution grid. References to the different forcing fields T_s, a_s, and q_{geo} are given in Table 1. PISM = Parallel Ice Sheet Model; TIAF = temperate ice area fraction; TIVF = temperate ice volume fraction.

velocities (Floricioiu et al., 2014). Diez et al. (2018) also imaged this feature and termed it the *Recovery-Slessor Gate*. Upstream of this point, the mountain range continues but shrouded beneath ice that increases in thickness until reaching the vicinity of subglacial lakes LA–LD. Lakes LA–LD and R9–R11 sit within a subglacial basin with ice ~3,000 - 3,500 m thick resting atop a bed ~500–1,000 m below sea level (Figure 2). A region of higher bed, with two subglacial peaks reaching >500 m above sea level (marked A and B in Figure 2), forms a ridge within the main upstream basin, possibly a further inland subglacial extension of the Shackleton Range. The mountain at *B* was also found by Diez et al. (2018) and Forsberg et al. (2018).

Following the main trunk from R9 downstream to the area denoted with E in Figure 2a, the ice thickness is in the range of about 3,000–3,500 m. At E the base forms a ridge about 1,000 m higher than its surroundings. This feature was also found by Diez et al. (2018) and Forsberg et al. (2018). Immediately downstream from this ridge and evidenced in the surface imagery (Figure 1) and subglacial topography (Figure 2b), a tributary joins the trunk from the west. Further downstream, at the junction with Ramp Glacier, the subglacial reflector deepens to >2,000 m below sea level, below ice >3,000 m thick. Downstream again, ~150 km upstream from the grounding line, the eastern shear margin ends, and Recovery Glacier becomes wider and turns eastward. Here the ice decreases to <1,500 m deep, with the bed lying below sea level at both margins. The western shear margin remains to just upstream of the grounding line, where the tributary Blackwall Glacier converges with Recovery Glacier, which together discharge ice ~1,200 m thick into Filchner Ice Shelf.

Ramp Glacier does not show any significant ice thickness variations along its main trunk. In its lower part Ramp Glacier cuts through valleys of both thin ice and high elevated bed, as is typical for an outlet glacier. However, neither the ice thickness nor the basal topography changes considerably in the upstream area marked with F. The sharp western margin of Ramp Glacier is thus unlikely to be topographically and might be driven by a change in sliding regime. An ice thickness variation of more than 500 m is found in Area G that appears like an ice-filled valley with a smooth surface in the radar imagery.

In contrast to Ramp Glacier's relatively flat profile, Blackwall Glacier varies considerably in ice thickness. It is thickest at its onset region, thinning downstream to match the thickness of Recovery Glacier where the two glaciers converge. We did not sound a basal reflector in the onset region, limiting a detailed interpretation of subglacial topography there, but in the vicinity is a deep subglacial basin. The main trunk of Blackwall Glacier has sharp shear margins imaged in the RES but appears not to follow a topographically defined route (Figure 2b).

With the new ice thickness measurements, the bedrock topography differs most visible for Ramp and Blackwall glaciers from Bedmap2 (see Figures S1a and S1c in the supporting information), because of previously
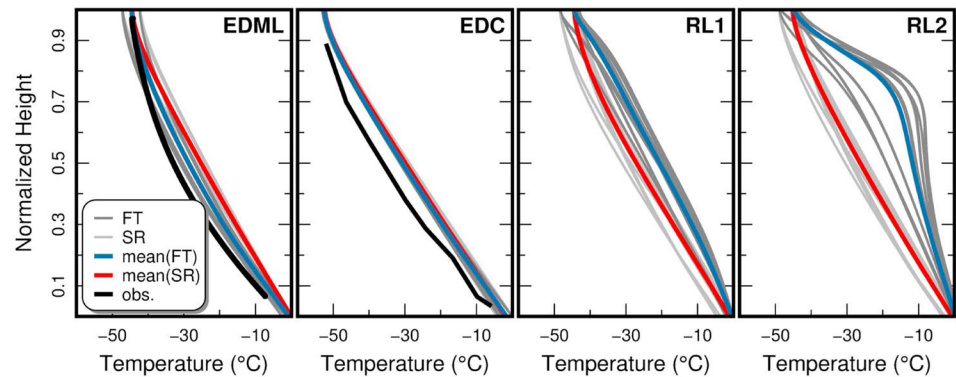
Figure 3. Comparison of simulated temperatures at selected locations. Observed borehole temperatures at EDML (Weikusat et al., 2017) and EDC (Zirizzotti et al., 2010) are shown in black. Thin light gray lines represent the different combinations of evoSR (SR) runs and thick dark gray lines the evoFT (FT) run. The mean of the presented evoSR runs is given by the red line and the mean of evoFT in blue. The sites RL1 and RL2 (see Figure 1) in the Recovery Lake area are located only 50 km apart. Note that the vertical axis is given as the height above the base normalized by the local ice thickness (base = 0, surface = 1). EDML = EPICA Dronning Maud Land; EDC = EPICA Dome C.

missing data. The bedrock topography inferred from ice surface terrain analysis by Le Brocq et al. (2008) differs from our data by more than 1,000 m in most areas (see Figures S1b and S1d in the supporting information). The largest disagreements are observed in the main trunk of Recovery Glacier with more than −2,000 m difference (R1, LA). In a large area between Recovery and Blackwall glaciers the bedrock is above sea level in our data set and below sea level in Le Brocq et al. (2008) with elevation differences of >1,000 m (bluish in Figure S1).

3.2. Subglacial Temperature Distribution

In general, the TIVF was very small, but locally the basal temperate ice layer thickness reached several 100 meters (Figure S2 in the supporting information). The results of all model runs are summarized in Table 2. The TIAF ranges from 17.6% for the lowest geothermal flux (q_{geo}^P) to 85.3% for the strongest geothermal flux (q_{geo}^F) for evoFT and from 24.7% to 88.7% for evoSR-type simulations. In general evoSR simulations resulted in larger areas that were temperate at the base. For the evoFT setup with the largest TIVF of 0.98% (T_s^{JCo}, a_s^{Ar}, and q_{geo}^F), the maximum thickness of the basal temperate ice layer was 374 m with a mean value of 20 m. The mean value was computed from all grid nodes with a temperate ice layer and not from all grid nodes. A larger maximum in TIVF of 1.13% was found for the evoSR setup (T_s^{FaO}, a_s^{VB}, and q_{geo}^F). Here the basal temperate ice layer thickness reached 308 m with a mean of 26 m. Individual runs showed grid nodes with significant thicker basal temperate ice (e.g., 761 m in setup T_s^{FaO}, a_s^{VB}, q_{geo}^F, and evoFT), but these runs did not result in the maximum TIVF as the area with temperate ice above was smaller. In general, thicker temperate ice was found in evoFT-type simulations.

To investigate the differences between evoSR and evoFT simulations, we present in Figure 3 temperature-depth profiles at two deep drill locations (European Project for Ice Coring in Antarctica [EPICA] Dome C [EDC], and EPICA Dronning Maud Land [EDML]) and two selected locations RL1 and RL2 in the Recovery Lake area (see Figure 1).

At EDC and EDML the simulated temperature profiles were in reasonable agreement with the borehole temperatures near surface and base, while they are systematically warmer elsewhere. The evoFT-type simulations match the observations at EDML better than evoSR-type ones, whereas at EDC the difference between both types of simulations is negligible. At this site, the different surface forcing (temperature T_s and surface mass balance SMB) data sets match each other very well.

While the observations show parabolic profiles, indicating downward advection, the evoSR simulations result in more linear (vertical diffusion dominated) profiles. The evoFT-type simulations result in implausible temperature profiles at RL1 and RL2, from which general conclusions can be drawn. The examples shown in Figure 3 for sites RL1 and RL2, located in the vicinity of LA, however, reveal slight and strong convex shapes. This indicates upward advection, especially at RL2. This is an obvious result of the flux correction applied to the SMB to match the fixed geometry, which is an interpolated quantity still based on sparse data. Thus, we focus on the evoSR-type simulations for further analysis of the model output.
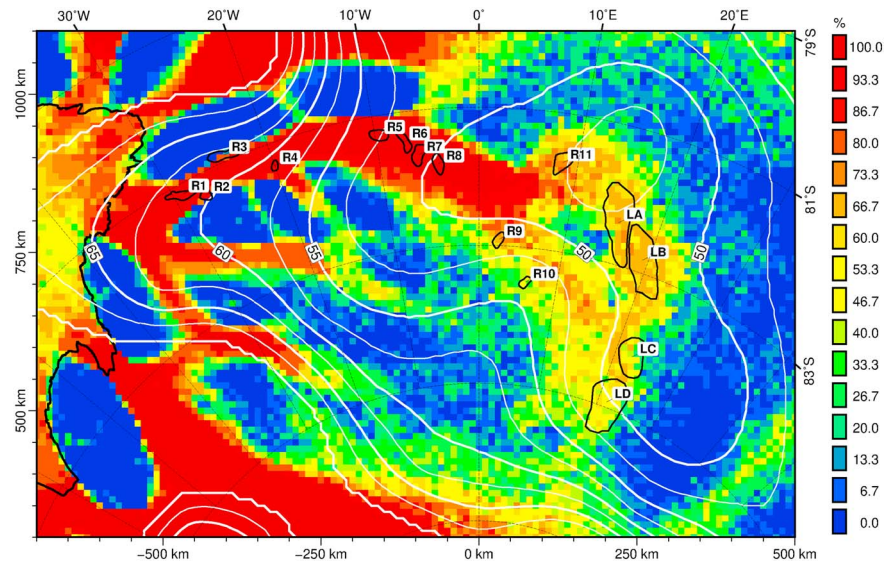
Figure 4. The occurrence of temperate ice at the base given in percent based on the 15 runs with a free evolving geometry (evoSR). Lake outlines and the observed present-day grounding line position are shown in black and gray, respectively. The mean geothermal flux is shown as white contours with 2.5×10^{-3} W/m^2 interval. The thick black line denotes the present-day grounding line position.

In Figure 4 we show the occurrence of temperate ice at the base, given in percentage of the number of evoSR-type runs. In the main trunk of Recovery Glacier approximately all runs lead to a temperate base, while in the area of LA and LB only approximately 10 out of 15 runs are that warm and the number of grid nodes at pressure melting point is further reduced at LC and LD. The distribution in Figure 4 for this lake area is strongly influenced by the very low heat fluxes from q_{geo}^P that are below 35×10^{-3} W/m^2. The subset of simulations with q_{geo}^P (Figure S3 in the supporting information) reveals that only very few grid nodes are temperate in just one out of five simulations. These grid nodes are located at LA and in between LA and LB. Further, we find that a temperate base is more likely downstream of LC than in the vicinity of LC.
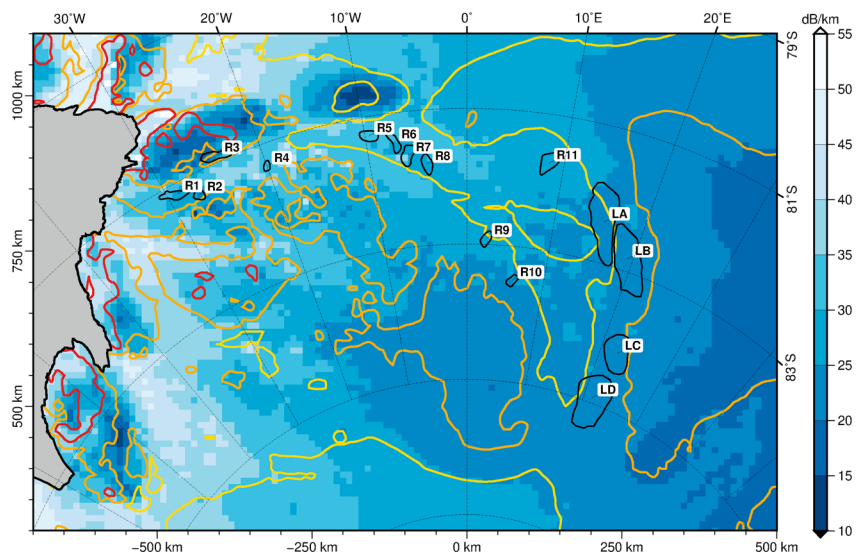
Figure 5. Depth-averaged attenuation rates (two way) derived from the simulated ice temperature fields based on the evoSR model ensemble for the pure ice attenuation model clipped at the present-day grounding line (thick black line). Selected contour lines at 2.5, 5.0, and 7.5 dB/km of the corresponding ensemble standard deviation are given in yellow, orange and red, respectively.
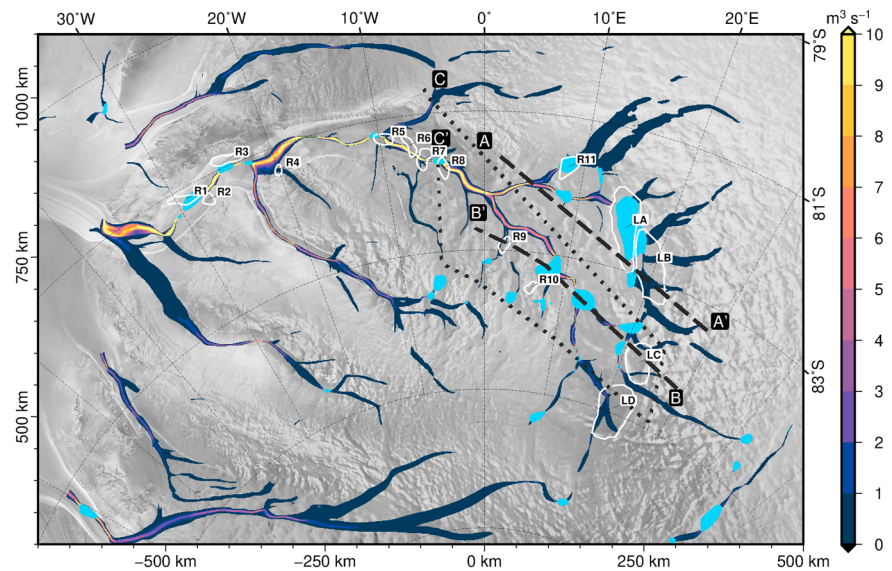
Figure 6. Magnitude of the subglacial water flux (m³/s) using catchment-wide melting of 0.006 m/a (clipped below 0.1 m³/s). Sinks in the hydraulic potential are shown in blue. Black dashed and dotted lines show the location of radio-echo sounding profiles shown in Figures 9–11.

The ensemble mean and standard deviation (STD) of the local attenuation rates (two way; see equation (5)) are shown in Figure 5 for the subset of evoSR-type simulations. These quantities have been derived from the modeled temperatures and the pure ice attenuation model given in Equation (7).

In the area of LA–LD, the attenuation rates are about 20 to 25 dB/km with STDs ranging from 2.5 to 5 dB/km. The attenuation rates increase downstream to ~30 dB/km with decreasing standard deviations (<2.5 dB/km) in the area of R5–R8. Attenuation rates up to about 40 dB/km are found between 15°W and 25°W. Largest STDs appear near the present-day grounding line, as the individual model runs result in different grounding line positions. Considerably larger attenuation rates can be found in the vicinity of the grounding line for Slessor and Support Force Glacier, the two large ice streams next to Recovery Glacier.

For a broader picture, the ensemble means and standard deviations of the attenuation rates are also given for the entire Antarctic Ice Sheet in Figure S4 in the supporting information. On the continental scale it becomes even clearer that the simulated attenuation rates in Recovery Glacier are lower than along the grounding line of most other ice streams and outlet glaciers.

3.3. Subglacial Water Flux and Hydraulic Potential

The modeled subglacial water flux and locations where sinks in the hydraulic potential have been filled are shown in Figure 6. Note that our subglacial topography in Figure 6 specifically records the ice bed (upper lake surface - we have no information from the RES of the possible lake depths). While we did the routing with all available basal melt rates from PISM (evoSR q_{geo}^S, q_{geo}^P, q_{geo}^F), we only show the result for catchment-wide melting at 0.006 m/year. The results using the PISM melt rates show the same flow pattern as the catchment-wide melt variant, albeit with much-reduced water flux and can be found in the supporting information Figure S5. A large portion of the water in the catchment drains along the main trunk of Recovery Glacier, reaching the sea at the grounding line. The modeled subglacial water flux varies in width and strength along the main trunk. Three medium sized sinks are present near the junction of Blackwall, Ramp and Recovery glacier. Close to S81°S, W010° there is another sink which matches the position of R5 (see Figure 1), but has only about a quarter of its size. The same applies at R8 upstream.

Further upstream, in between point A and point B′ the subglacial flow branches. The northern branch drains lakes R9 and LA. Both coincide with sinks observed with our model. In addition two smaller sinks were found. LB does not appear in our model as a sink. However, a nearby small sink is found. The southern branch drains pathways upstream LC and LD. We do not find any sink in the potential across both lakes. However, a number of smaller sinks are found in the vicinity. R9 and R10 do not appear in the hydraulic potential, though we find sinks slightly offset westward. The RES section B-B′, shown in Figure 10, runs across two larger sinks located
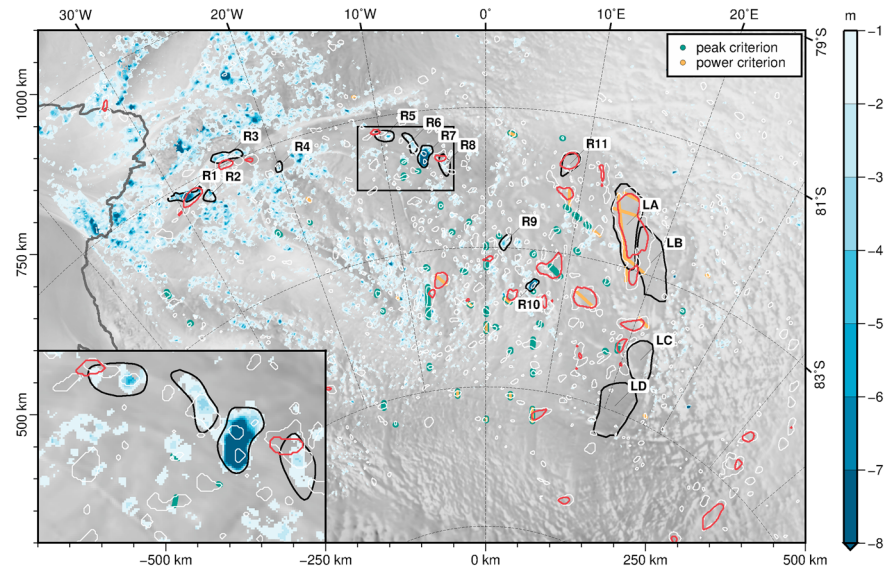
Figure 7. Elevation anomalies identified using ICESat. Shown are lake drainage events as integrated negative anomalies with a blue color scale. Results of the lake classification scheme are shown as green dots along the flight profiles. Sink contours derived from the flux model are shown as closed polygons in light gray for the 2 km and in red for the 10 km smoothing kernel.

between LC and R9. Panels (a) and (b) of Figure 10 show the water flux distribution and hydraulic potential between the lakes. We find moderate flux along Blackwall Glacier and a small sink far upstream. Also, Ramp Glacier is underlain by a water stream. However, no sinks are found. At the upstream end of Ramp Glacier one medium and one small-sized sink are located.

Flux computed with the melt rates from the evoSR PISM simulation using q_{geo}^S (representing a moderate geothermal flux) is—as expected—much less and large areas have flux below 0.1 m^3/s and are therefore clipped (see Figure S5b in the supporting information). However, the main drainage path is still active and contributions from Blackwall and Ramp are present. Almost all identified sinks are still connected to the drainage path, with the exception of the upstream Ramp Glacier. Also, at the previously known lakes R9 and R10 almost no flux is visible. Using q_{geo}^F, the distributions of flux and sinks are nearly similar to q_{geo}^S, but for q_{geo}^P the water extent is strongly reduced (Figure S5 in the supporting information). To investigate the sensitivity of the flow patterns to errors in the topography, we disturbed the ice surface with a random variation of 1 m and the ice base with a variation of 25 m. The general pattern is very stable, and only individual segments of the flow network have reduced flux or vanish.

3.4. Active Lakes From Altimetry

Figure 7 displays color coded integrated negative elevation anomalies derived from ICESat laser altimetry (see Figure S6 in the supporting information for positive and total anomaly maps). The distribution clearly indicates areas with large elevation anomalies in the main trunk of Recovery Glacier at locations R1, R7, and R10. Those anomalies have been previously interpreted as lake drainage events with a subsequent refilling (Fricker et al., 2014; Smith et al., 2009). The inset shows a zoom in to lakes R5 to R8 which were described as

Table 3
Indication of Existence of Lakes Based on 1-D and 2-D Lake Candidates and a Relative Power and PPC Criteria

Criteria	1-D approach	2-D approach
Number of lake candidates	483	192
Relative power criterion	55	24
PPC criterion	173	44
Relative power and PPC criterion	23	7

Note. PPC = peak-to-peak correlation.
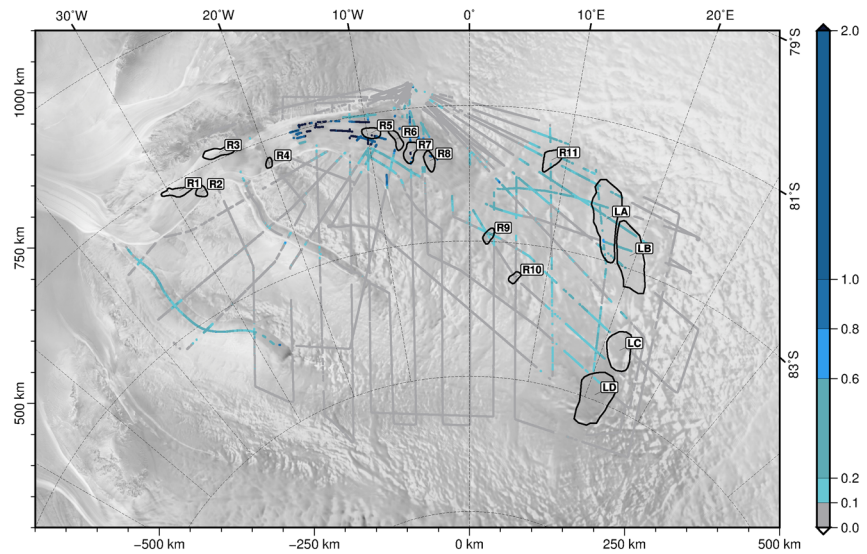
Figure 8. Basal reflection coefficient r. Colors denote likely dry regions (gray) and swampy to wet (turquoise to blue).

a connected system of active subglacial lakes (Fricker et al., 2014). The figure also demonstrates the limit of this technique since erroneous anomalies are found in areas with steep topography, at grounding lines and over crevassed areas as discussed in Smith et al. (2009). Results of the two lake classification criteria described in section 3.5 are also displayed in Figure 7. While the match of one criterion is widely found at and around LA–LB and downstream, only a few locations where both criteria match are found. East of 0°E, the sinks found with our modeling match with at least one criterion for nine of the larger sinks, while only one does not match the two criteria.

3.5. Lake Identification
Results of the 1-D and 2-D lake identification schemes are given in Table 3 and for 2-D in Figure 7. Both approaches show very different results. With the 1-D method over twice as many lake candidates were identified (which was expected, since the 2-D method is a stricter condition). In both cases the candidates are distributed across the whole area, representing localized hydraulic sinks. Marked discrepancies between the two approaches are found across LA and LB. Here the relative power criterion is fulfilled for the 2-D approach nearly across the whole area, whereas candidates from the 1-D approach do not match any criteria. This location is covered by five flight tracks. In addition, any of the criteria for both approaches across lakes R5 to R9 do not match, whereas R10 at least partly fulfills the basal reflectivity criterion in the 1-D approach.

3.6. Basal Reflection Coefficient
As discussed above, we are limited with our capability to determine the magnitude of r with sufficient certainty. Nevertheless, we interpreted low values of r as an indicator of a dry base (gray, $r < 0.1$) and high values for a wet base, respectively (blueish). This assignment was decided from the range of r shown in the right panel of Figure 8. While the absolute values strongly depend on the estimated absorption, the general pattern of the distribution remains unaffected by that. According to this indicator, most of the base of the study area is dry, in particular, all areas outside the main trunk of Recovery, Ramp, and Blackwall glaciers. Downstream of the southern end of lakes LA–LD, the basal reflection strengths ($r > 1$) are indicative of a wet base underlying the main trunk of Recovery Glacier. Using 0.1 as a rather conservative threshold, this distribution (Figure 8) suggests that there are two branches in the upstream Recovery Glacier: (i) R10, LA, and LB and (ii) LC/LD, which are separated by a dry bed. Blackwall Glacier is most likely resting on a wet bed, while results for Ramp Glacier are ambiguous, as along and across flow profiles show different magnitude of r. This is likely related to the narrow valley geometry. The general pattern is similar to the distribution of the simulated temperate base and potentially driven by the effect of temperature on the absorption.

3.7. Combined Analysis
We have selected three profiles for which we show a multitude of variables (water flux, hydraulic potential, temperate layer thickness [Hcts], basal homologous temperature, absorption, ice thickness [H], reflection
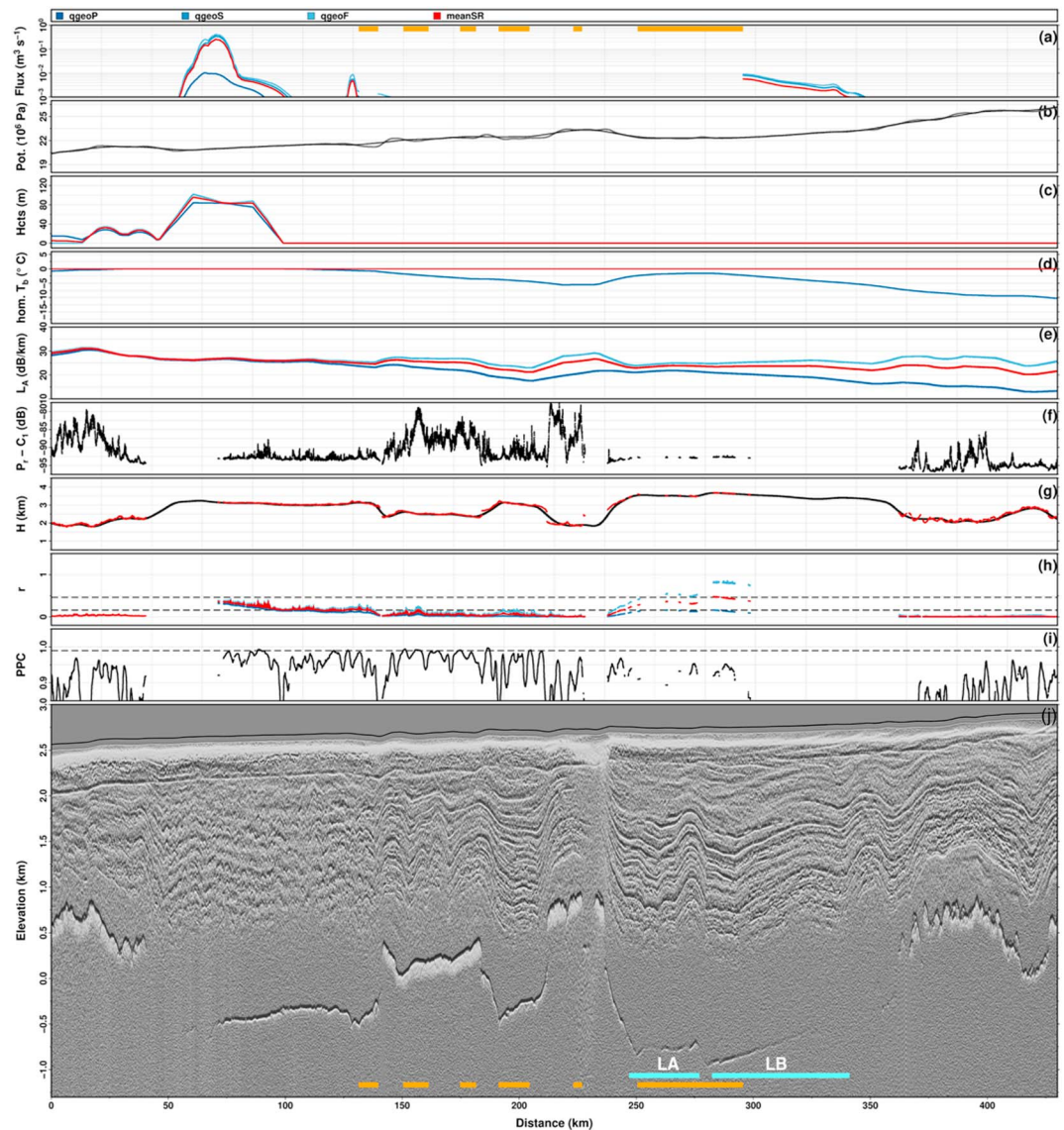
Figure 9. Section A-A′, running from northwest to southeast, covering southern part of LA and LB (see Figure 6). The panels show the following: (a) water flux (generated using the 10-km smoothed potential), (b) hydraulic potential, (c) thickness of the temperate layer, (d) basal homologous temperature, (e) radar attenuation—averaged over 1 km, (f) received signal power reduced by the factor C_1 for comparison with Langley et al. (2011), (g) ice thickness-semiautomatic picks (red) and new ice thickness grid (black), (h) basal reflection coefficient, (i) peak-to-peak correlation, and (j) the processed radargram with static correction applied. Superimposed on (j) are the crossing of either formerly proposed lakes (light blue) or sinks in the two-dimensional hydraulic potential arising from this study (orange). Within the other panels, the blueish colors represent different geothermal heat flux distributions of the evoSR ensemble, while red represents their mean.

coefficient, and PPC) in Figures 9–11, with the aim of providing insight into the factors that influence the determination of r. This is the basis of a general discussion to determine r. For comparison with the studies of Langley et al., (2011, 2014) we also calculated $P_r - C_1$ (geometrically corrected bed reflectivity), which corresponds to their $\delta[P_{bed}^c]_{dB}$. The profiles cross existing lake outlines as well as modeled potential lake sites.

A static correction has been applied to the radargrams presented in Figures 9–11 using the Bedmap2 surface topography (Fretwell et al., 2013). The upper strong reflectors indicate the ice surface. Below the surface, internal layers, dips, as well as crevasses are visible in addition to a multiple of the surface reflection. Further down, usually a single strong reflection stands out from the background noise. This is interpreted as the bed reflection and indicates a strong dielectric contrast.
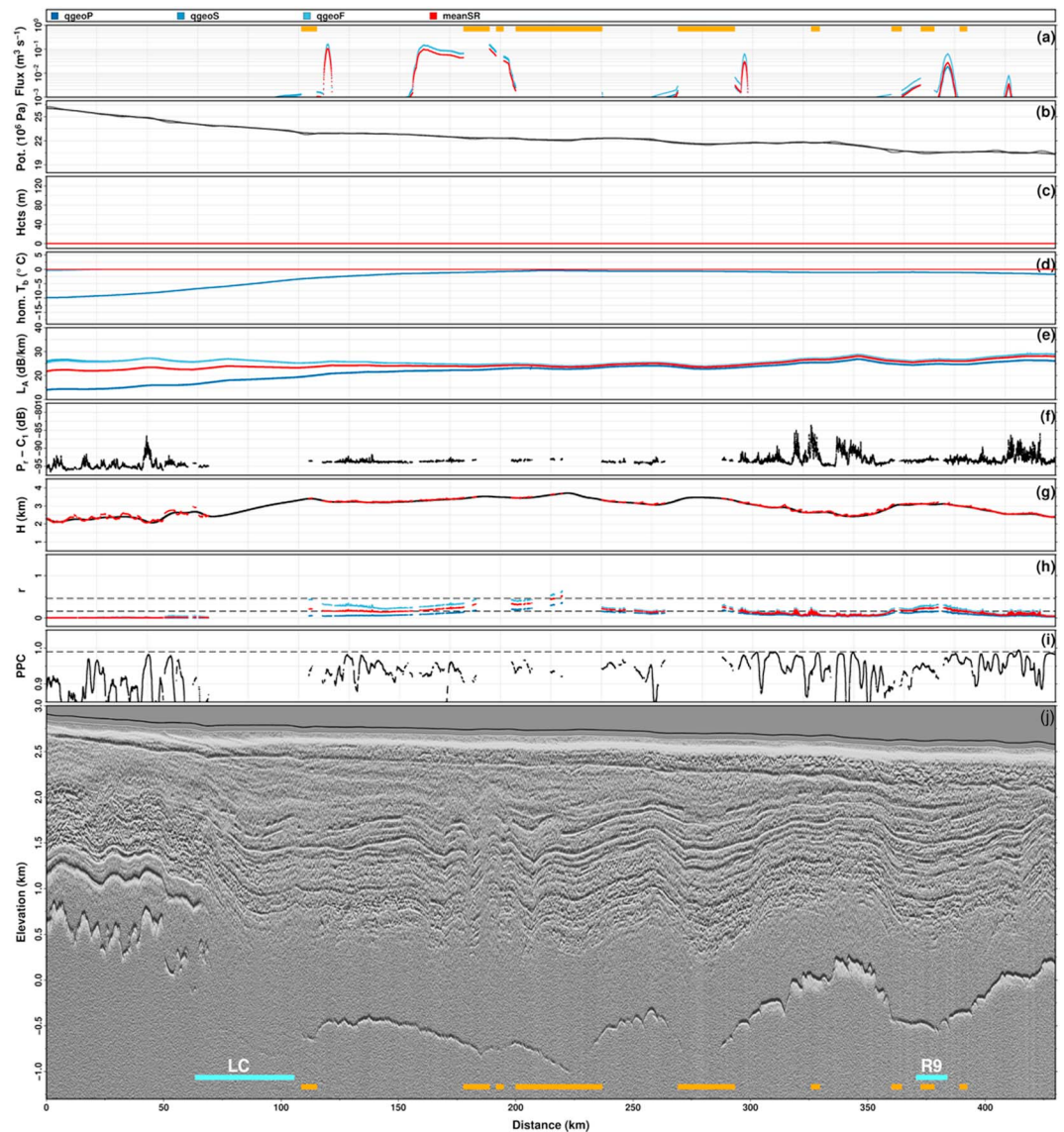
Figure 10. Section B-B′, covering lake C and lake R9. See Figure 9 for description of the panels.

The radargram in Figure 9j was recorded on a 430 km straight flight line (A-A′ in Figure 6), at a constant flight level crossing the southern parts of LA and LB at km 247 to km 344. The ice thickness in this profile varies between 1,700 m just west of LA and nearly 3,700 m at the western edge of LB (see Figure 9g). The detected internal layering is less pronounced and slightly disturbed in the first third compared to the rest of the profile. This matches the onset of the ice stream, where we observe higher melt rates (see Figure 6) and high probability of temperate ice at the base (see Figure 4). Close to the middle of the profile, around km 237, the internal layering is disturbed by a band of increased noise, caused by surface clutter originating from (near) surface crevasses. The clutter is formed right at the edge of a nearly 2,000 m high step in the topography of the ice base. Basal reflections were obtained for most parts of the profile. However, two larger breaks of about 20–30 km each and several shorter gaps occurred. The shorter gaps are most likely caused by steep bed topography. The internal layering above the first section without bed reflections (approximately km 43–69) indicates that the beginning of a steep depression might be located here, which would lead to off-nadir reflections. This is followed by an area where a substantial temperate layer at the base might form a region with gradually increased attenuation and thus reduces the dielectric contrast between ice and underlying bed. The flux routing (see Figure 9a) shows high water flux underneath parts of the modeled temperate ice layer, which partly compensates for the larger absorption so that basal return power increases. The disappearance of basal
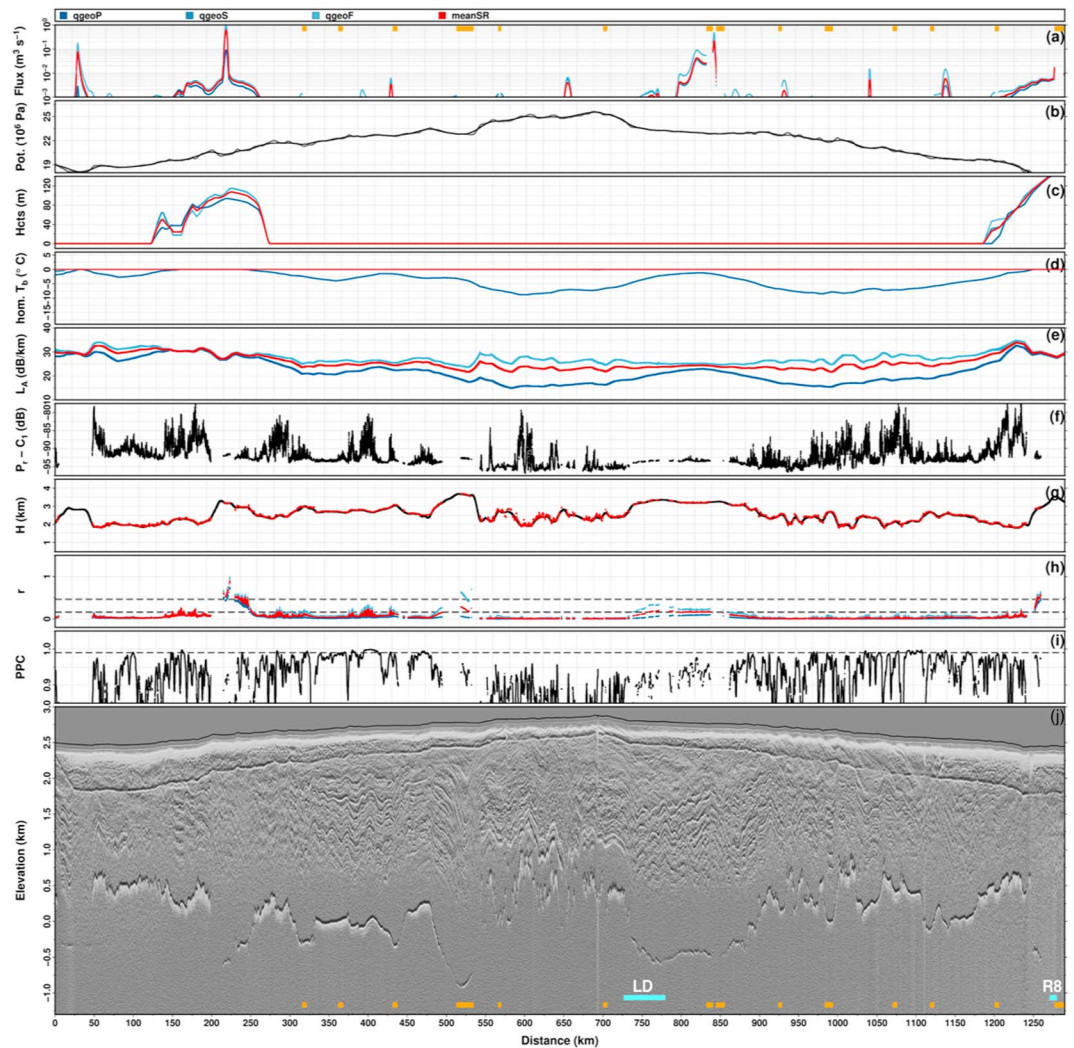
Figure 11. Section C-C′, covering the northeast of LC, LD, as well as R8. See Figure 9 for description of the panels.

returns at the eastern part of LB is quite striking, even though the bed seems to rise more than the surface. The change in reflectivity (Figure 9h) coincides with decreasing basal water flux (Figure 9a). The internal layering points toward a rising bed followed by a steep peak before reflections show up again, revealing a range of about 40 km in length, about 350 m higher than its surroundings, and several valleys about 100 m below the peaks of this range. Our data show that LA and LB are separated by a step in the bed of about 200 m. Next to this step, we find a sink in the hydraulic potential. The internal layering in this part of the profile inclines in profile direction toward southeast, while the bed rises, making the inclination of layers likely to be due to melting. The geometrically corrected basal amplitudes reveal large variations of about 10 dB along the section. These variations are least pronounced across LA and LB and extend further than the basal water flux would indicate. No model run shows a temperate layer from km 271 onward (see Figure 9c), while the base is always temperate (except for q_{geo}^{P}). The derived reflection coefficients indicate the existence of a lake centered between LA and LB (around km 275 to 290; see Figure 9h).

The second profile B-B′ (see Figure 6 for the location) is shown in Figure 10j. It is also about 430 km long and covers the area about 100 km south of the profile A-A′. It crosses LC (km 65 – 108) and turns north close to km 301 before crossing R9. At the onset of the profile, up to km 60, basal returns reveal an undulating bed overlain by approximately 2,400 m thick ice. Across LC no clear basal reflections were obtained. Just west of the lake, basal returns reappear and reveal a relatively smooth bed covered with 3,000 to 3,500 m thick ice. Two larger

gaps in basal returns are located around km 232 and 275. Due to the quality criteria for the evaluation of the reflection coefficient, the picks between km 185 to 198 do not show up in panels (f), (h), and (i). From km 288 to km 348 the bed rises 1,000 m, followed by a 700 m-deep depression with a width of about 50 km.

The profile crosses nine sinks in the hydraulic potential (see orange bars in Figure 10j). Their width varies between 3 and 37 km. None of them intersect with LC but one with perhaps half the width of Lake R9. However, neither the extracted reflection coefficients in panel (h) nor the internal structure of the RES section shows clear indications for subglacial lakes at these locations.

The internal layering above LC shows downwarping, but this is most likely caused by the depression and not by basal melting. Above the troughs, around km 280 and 376, the internal layering also follows the bed. Between km 198–215 the internal layers bend down while the bed dips down. This could be caused by basal melting. The section is located just above the western part of the largest sink in the hydraulic potential. The reflection coefficient r in panel (h) of Figure 10 reaches values close to 0.5 above the large sink, indicating the presence of water at the base of the ice sheet. However, the spread for r, calculated using different geothermal heat flux assumptions, is relatively large compared to sections at the beginning and end of the profile. For reflections above lake R9 r reaches values between 0.1 and 0.3 which indicates the presence of a swampy bed.

The third radargram shown in Figure 11 (1,285 km long, C-C' in Figure 6) covers the northeast of LC and crosses LD, as well as R8. The ice thickness along the profile varies between 1,645 m (around km 1,017) and 3,685 m around km 516, revealing a highly undulating bed (see Figure 11g). Along the first 500 km the ice thickness increases from about 1,800 to 3,000 m with multiple troughs in between. The deepest trough (km ∼215) exhibits an elevation difference of about 1,000 m with a slope exceeding 10%. The largest ice thickness is found north of LC, approximately 50 km before the profile turns southward. The section east of LC reveals a plateau in the bed below 1,800- to 2,800-m-thick ice. Where the profile crosses LD (km 731–783), it exhibits a declining bed followed by an ∼150-km-wide depression. Between km 903 and 1,075 another strongly undulating elevated bed under 1,800 to 2,800 m thick ice is found. This is followed by two more troughs in the north and by a rising bed toward the ice stream. At the southern edge of the ice stream the bed suddenly drops by more than 1,000 m, from where on no returns were obtained from the center of Recovery Glacier and across lake R8.

The 14 sinks we found in the hydraulic potential are 10–25 km in width and are distributed over the whole profile, starting at km 314 (see orange bars in Figure 11j). One sink overlaps with lake R8, but none matches LD. The section crossing the largest sink, centered around km 525, shows steep inclined internal layers dipping into the trough. Since the slope of the layers does not decrease with increasing distance to the bed, this points toward a section with basal melting. The corresponding r for this segment of the RES profile indicates a swampy bed (see Figure 11h). There are three more sections with increased r. For example, in a depression around km 215–237, which precedes a deep valley, values of 0.5 and higher are reached. Flux routing (see Figure 11a) also shows a considerable amount of water passing through this region, and our modeling reveals a temperate layer which is up to 100 m thick (see Figure 9c). The second segment coincides with LD with values of r around 0.2, and at the southern edge of the ice, a short section reveals values of r around 0.5. Directly above LD, no water flux was found, but downstream larger amounts of basal water are present according to our modeling (see Figure 9a). The edge of the ice stream is another region in which the basal water flux and an extensive layer of temperate ice with a predicted height of at least 120 m occur. This is most likely the reason for the loss of basal returns in the ice stream. Between km 280 and 430 three shorter segments with increased r show up. Two of them, around km 409 and 430, exhibit a large PPC and noticeable basal water flux (see Figures 11a and 11i).

4. Discussion

4.1. Origin of Missing Basal Reflections

The distribution of the ice thickness picks shows (see Figure 1) that we partially lose basal returns in the main trunk of Recovery Glacier. While the deployed RES system sounded ice of more than 3,700 m thickness (detected maximum: 3,759 m) in the surveyed area, no returns were received in regions where much thinner ice is expected. This could be caused either by a technical problem or by the fact that not enough energy is reflected. The latter can be caused by large attenuation within the ice or a lack of dielectric contrast (permittivity and conductivity).

There are no hints for technical problems such as a sudden increase in noise level or decreased TX power. Both were checked by examining the noise floor at the end of the registered shots, respectively, the direct signal between the antennas.

In regions with horizontal layering signals are reflected to the antennas. Ice flow disturbs the layering and creates crevasses, off-nadir scattering occurs, and no returns are detectable, because only a fraction of the energy is reflected to the antenna. This is most likely the case for the glacier section west of 17°W. Furthermore, a large amount of energy is reflected at the ice surface in regions with surface disturbance, such as surface crevasses. In that case, only a fraction of energy penetrates into the ice while the reflected energy is registered as noise. Steep bed topography also causes potentially nonnormal incident reflections.

Since the attenuation of electromagnetic waves in ice is a function of temperature and frequency (Bogorodsky et al., 1985; Robin et al., 1969), the signal level can be reduced below the detection limit of the system. The two-way attenuation of ice at a 150 MHz varies exponentially between 1.2 dB/km at −60°C and 49 dB/km at −1°C (Robin et al., 1969). Thus, warm ice above wet beds might be the cause for vanishing basal reflections, also suggested by Siegert et al. (2014). This is a potential explanation for the lack of reflections in the region of LA–LD and R5–R8 and upstream.

Another reason for the absence of reflection might be a gradual transition with a mixed layer with varying components of ice and sediments between the ice sheet and the bed. Dry sand, limestone, and other geological materials have a permittivity only slightly larger than ice (Davis & Annan, 1989). Thus, a mixture might not produce a contrast large enough to cause a noticeable reflection. However, water-filled sediments have a larger dielectric constant which would result in a power reflection coefficient of 0.18 at the base of the sheet for normal incident signal.

Finally, the presence of a layer of temperate ice might suppress basal reflections. The microscopic water content within the ice changes the dielectric properties, according to a mixture theory, where a very small water content has a strong effect. As the water content within a temperate layer changes continuously and on small rates, a smooth transition of the dielectric constant from pure ice to water might prevent a strong reflection at the bed. In this case, only the cold to temperate ice transition would cause a reflection. However, also the increase in absorption itself may cause the loss of the basal return if the transmitted power is not sufficiently large.

The above-mentioned reasons in addition to findings of Siegert and Bamber (2000) indicating a lack of subglacial lake signals over relatively thick ice in East Antarctica lead to the conclusion that within the deep main trunk of Recovery high attenuation rates and a temperate ice layer are likely to be expected. This is supported by our modeled ensemble of attenuation rates to be highest in the fast flowing regimes of Recovery, Ramp, and Blackwall Glaciers (see Figure 5). A combination of large ice thickness and high attenuation rates as observed in the Recovery trunk prevents energy reflected to the radar, no matter the bed conditions.

4.2. Missing Evidence in Lake Identification

It has been proposed that subglacial lakes appear as bright, flat, specular reflections, typically 10–20 dB stronger than reflections from the lake's surroundings (Siegert & Ridley, 1998). To provide such large dielectric contrast, a thick body of water (>10 m) is required (Christianson et al., 2012; Siegert et al., 2014). Gorman and Siegert (1999) showed that RES systems may even be capable of detecting both interfaces of a body of water: the ice water and water bed transition. The maximum detectable water thickness is limited by the high attenuation of electromagnetic waves in fresh water of 119 dB/km (Hippel, 1958) to about 20 m (Gorman & Siegert, 1999). Based on a simulation by Christianson et al. (2012), the minimum resolvable layer thickness is about 6 m. They state that thinner water layers produce a composite echo similar to single bed reflection. The minimum layer thickness for a burst RES system depends on its burst length, which is 600 ns for the AWI-RES system. Thus, the AWI-RES system does allow the detection of water bodies but not its thickness.

In our analysis we followed Oswald and Gogineni (2008) and estimated the integrated reflectivity to minimize the high along-track variability of the bed reflectivity (up to 10 dB) which has been shown to prevent clear lake identification in a series of RES studies (e.g., Siegert et al., 2014; Wright et al., 2012). Our results show a reduction of the variability (standard deviation across the Fresnel zone) by averaging along track and a further reduction using the integrated power. However, concerning the relative power analysis between lake and lake surroundings (Carter et al., 2007), one can observe that relative integrated power ratios are also minimized, which counteracts the positive effect of minimizing the Fresnel zone variability. Therefore, our results show

that the use of the integrated power suggested by Oswald and Gogineni (2008) cannot reduce the uncertainty in the power criterion.

Our findings of high along-track variability of the bed reflectivity are also in line with a detailed analysis of an active lake (Institute E2) using RES data (Siegert et al., 2014). They found that the RES was not able to clearly prove the existence of a deep (>10 m) water body, although ICESat analysis revealed a 6 m uplift 2 years before the airborne survey. However, they found areas with considerably higher (10 to 20 dB) basal reflectivity next to a strong along-track scatter in the vicinity of the lake center, suggesting but not proving the presence of water. Christianson et al. (2012) found a sudden 6 dB increase in a very detailed RES survey across the active subglacial Lake Whillans. The zone of higher reflectivity, found to be in the vicinity of the hydraulic low underneath a 15-m surface depression, indicates wet basal conditions but no clear evidence of a thick (>6 m) water body. Despite those known difficulties, but encouraged by the study of Carter et al. (2007), we applied the lake identification scheme to our data set. Our analysis was hampered by the absence of bed returns or low signal-to-noise ratio in or low signal/noise ratio in the main trunk of Recovery Glacier and in the vicinity of the Bell lakes LA–LD as explained in section 4.1. In consequence the 1-D along-track lake classification is limited to areas with a clear continuous bed reflection with low small-scale variability of the basal reflectivity. To overcome the limits of the 1-D along-track analysis, we applied a 2-D approach making use of the continuous spatial coverage of the newly derived ice thickness grid (shown in Figure 2a) as input to determine the hydraulic sinks as lake indicators. Since a few automatic picks are available also in the mentioned problematic regions, the means of the two criteria can be estimated and used for the lake identification in the 2-D approach. Our findings show an inconsistency between both approaches. A clear indication that relative power or basal reflectivity can be used as a reliable criterion over a large region supported by both approaches was not found. We conclude that in our survey the basal reflectivity cannot be used as reliable parameter to distinguish between dry and wet beds (even across clear lake-like reflections), due to its high spatial variability. Another study of Wright et al. (2012) applied the Carter scheme to the ICECAP survey across the Aurora basin in West Antarctica. To obtain basal reflectivity, the received signal strength was corrected for geometric spreading and attenuation rates estimated using the GLIMMER model and Dome-C ice core chemistry. In addition, the basal reflectivity was calibrated at the known Lakes Concordia and Aurora, which were crossed during the survey. The offset of 25 dB was simply added to the data set to bring the data in line with typical values for wet conditions (Peters et al., 2005). However, an offset of 25 dB suggests a higher attenuation rate as the modeled one, which in turn would change the distribution of the estimated basal reflectivity. Furthermore, Wright et al. (2012) showed a radargram across Lake Concordia in connection with the estimated basal reflectivity. Here a spread of 20 dB across the flat lake-like reflection was found. In addition Wright et al. (2012) observed only a couple of lake-like reflectors which are classified as fuzzy or dim lakes. Their results are similar to those we have presented, which question the reliability of the method based on basal reflectivity, to be able to distinguish between wet and dry beds and/or to classify lakes. Siegert et al. (2016) confirm this observation of a lack of evidence for deep pooled water in those active regions. Siegert et al. (2014) conclude, based on the incapability of RES to detect thin water bodies, that the level of stored water in Antarctica may be significantly underestimated. However, it can be argued that if RES is unable to provide clear evidence of existence and extent of water bodies, one cannot draw any conclusions on overestimation or underestimation of the water volume at all.

4.3. Trustworthiness of the Basal Reflection Coefficient

The absorption rate based on ice modeling can be estimated in different ways, each with their own assumptions and pitfalls. Having found that the freely evolving ice thickness results a more reasonable ice temperature profile, we are able to account for differences in the modeled and observed ice thickness. There are different ways that are conceivable and that were all tested: One can estimate (i) the absorption rate at each location and apply this to the ice thickness found in each shot (this is the basis for r in Figures 9–11) or (ii) to the ice thickness grid or (iii) correct for the ice thickness anomaly. With ice thickness anomalies up to 300 m this could make up to 10 dB difference in the absorption at a particular location and is hence in the order of the variation of $P_r - C_1$. Even if we were able to get a better match between modeled and observed ice thickness, we would still be unable to specify the contribution of impurities on the absorption because the nearest deep ice core is far away from the study area. Therefore, the ability to estimate r is low, despite our extensive modeling effort. Further complications arise from the fact that the performance of the AWI-RES system is too low and no phase information is recorded.

However, on the premise that our modeled temperature field gives a reasonable basis of the spatial variation of $L_A(T)$ assuming that neither impurities nor ice thickness anomalies cause sudden changes in absorption, we can interpret the spatial distribution of r. This distribution is affected by the temperature in the way that overestimation of L_A due to overestimated temperatures leads to overestimation of r, and thus, low values of r are safe to interpret.

Thus we conclude that upstream of LA–LD, we find no indication for subglacial water by means of radar and temperature modeling. There is no indication that ice in the main trunks of Recovery Glacier or Blackwall Glacier rest on a dry base. The distribution of r (Figure 8) downstream of LA–LD suggests the presence of two branches separated by ice frozen to the base.

Along the profiles the spatial variability of r is rather low (see Figures 9–11)—dry areas extend over tens to hundreds of kilometers. This also justifies the scale of the filter used for the flux routing. Larger values of r coincide with high small-scale variability. Although we do not have an absolute measure for r, we conclude that the variability in a wet basal system is high. We expect wet sediments, cavities, and thin sheets alternating on spatial scales below 10 km.

Comparisons of our results with the findings of Langley et al. (2011) show similar variations in amplitude of the geometrically corrected P_r, but the geographical distribution has changed since their measurements during the Norwegian-US IPY traverse. Both data sets show relatively large corrected P_r values across LA and LB. While we found that r was almost at the same level outside of LA, Langley et al. (2011) observed a decreasing trend of r in direction R11. This could be a hint for a change in subglacial conditions in the vicinity of R11 between both campaigns.

R10 was originally proposed by Smith et al. (2009) based on elevation change, and this has been confirmed by Fricker et al. (2014) using the same data basis of ICESat. We also found an elevation anomaly based on ICESat repeat-track analysis. In contrast, r consistently indicates a dry base for all model ensemble members, with P_r being clearly above the noise level. Although we do find a hydraulic sink with the 2 km filtered hydraulic potential, it is not present with the 10-km filter, making its presence less likely. The base is cold for all ensemble members of q_{geo}^P and only temperate for a few ensemble members of q_{geo}^S and q_{geo}^F. This is a further indication that the base is dry. Last but not the least, the radargram does not exhibit a lake-like reflection and no match with the lake classification parameters. The flight profile in flow direction across the lake shows a step in the basal topography and internal layers above that are dipping down. This is difficult to interpret. A lowering of the ice surface would be consistent with a lake that drains to the extent that it would become dry. However, it is inconsistent with the hydraulic potential that is based on reasonable data. Similar to the study of Wright et al. (2014), our findings are consistent with criticism of interpreting surface lowering as a definitive indicator of lake drainage.

Jacobel et al. (2010) found high local variability in relative basal reflectivity. Those variations are only in some areas in line with a flat-lying bed reflection indicative for water. They used a constant one-way attenuation value of 8.6 dB for the entire 1,700 km long US-ITASE traverse covering a large area from South Pole to Taylor Dome. They correlated surface velocity with relative basal reflectivity and found good correspondence between areas of high basal reflectivity and ice speed only in portions of the Byrd Glacier catchment, whereas one third of the traverse showed high reflectivity in areas of low speed. Their results indicate a widespread wet bed in East Antarctica. In the analysis of Jacobel et al. (2010) and Oswald and Gogineni (2008) a double Gaussian model is fitted to the whole reflectivity ensemble. This approach is based on the assumption of the existence of a statistically significant amount of water in the area of investigation and lacks a spatial varying attenuation rate which would significantly change the form of the histogram. Given our modeled absorption rates (see Figure S4), we developed a more critical view on the ability to distinguish between wet and dry basal conditions, which is supported by Diez et al. (2018), who demonstrated the enormous effect of varying attenuation rates from 0 to 10 dB on the relative bed return power across Slessor Glacier. This nicely illustrates also our findings that the Carter scheme, using differences between bed reflectivity across indicated lakes and its surroundings, is strongly affected by the applied attenuation rate, which is hard to constrain with reasonable accuracy. Diez et al. (2018) showed that in one case a significant difference between the Recovery Slessor Gate and its surroundings is observed and in the other case using lower attenuation rates not. Our modeled attenuation rates vary over a range of 45 dB/km in the Recovery area with uncertainties of up to 6 dB/km (see Figure 5). Diez et al. (2018) found ~15 dB decreased bed return power (only corrected for geometric spreading) for the Bailey Trough region compared to Slessor Glacier for depths of 2,500 m. The authors interpret this

difference to be caused by changes in basal properties and conclude a wet bed beneath Slessor Glacier and dry bed for the Bailey Trough. However, if we assume that this change is simply driven by a spatial change in attenuation rate, this would yield roughly 6 dB/km higher absorption in the Bailey Trough which is in line with our modeled rates showing a 5 dB/km higher rate. Based on those findings, no change in bed properties could be concluded.

This example emphasizes the importance of a better constrained attenuation rate including their spatial variability, which can vary over short distances easily by 5 dB/km (Figure S4). More importantly, attenuation rates are essential to estimate basal reflectivity from RES data and which in turn are widely used to characterize subglacial conditions. Whether the reflectivity indicates a dry or wet bed, has a strong impact on the overall ice flow dynamics. Therefore, this is a crucial parameter that needs to be considered very carefully.

4.4. Synthesis

Our analysis of P_r to estimate the basal reflection coefficient was not successful, and we were able to rule out technical problems of the radar system as the cause. It appears that the absorption of the ice is larger than expected from the ice thickness alone. This is consistent with the temperature distribution found in our modeling. Despite the large uncertainty due to the error in the geothermal heat flux, it becomes clear that the ice stream consists of relatively warm ice. Although we can neither infer the basal reflection coefficient nor any lake indicators, it is most likely that the main trunk of the ice stream consists of a wet base.

By modeling the temperature field, we were able to derive the regionally variable ice absorption rate. This enabled us to understand that we are equally limited by the absorption in the ice, as by the transmitted radar power. The spread within the model ensemble members clearly demonstrates that ensembles are required to obtain a basic measure of uncertainty.

The hydrology model provided additional hints on possible subglacial lake locations. Two of the lakes (LC and LD) do not coincide with our sinks, two (LA and LB) appear as a single sink. Furthermore, various smaller sinks exist in the main area of the ice stream as well as in two interconnected chains merging with the main trunk. The simulations using the modeled basal melt rates showed that water is only available in a limited area. While our hydrological model proposes a layer of water below those areas that have higher velocities, the limited extent of the water layer upstream of R5–R11 does not allow us to conclude that massive amounts of subglacial water are the driving force behind the ice stream genesis of the Recovery Glacier. Nevertheless, sliding plays an essential role, as well as the deformation within an extended temperate layer of ice, as shown by our ice model.

We have checked all our radargrams for the appearance and disappearance of internal layers with the purpose to use this as additional information about the flow behavior of Recovery Glacier. We found that the area down to 0°E/W shows a layered structure down to the lower third or quarter of the ice thickness. In this respect, Recovery Glacier is similar to the North East Greenland Ice Stream as shown in Vallelonga et al. (2014). Layers within the ice are supposed to lower, once ice flows across a subglacial lake, as shown in Gudlaugsson et al. (2016) and Leysinger Vieli et al. (2007). There is no change in the layered structure upstream or across the large lakes (see Figure 11). At other locations, where there is remarkable downwelling of layers, a basal step is linked to the dipping of layers, like around km 516–538 in Figure 11.

Reversing the approach, we can check how flat the base of the ice stream is at locations where the large lakes are proposed. Our flight routes were chosen so that we also cross lakes in the direction of flow. Given the large extent of the LA–LD, the ice base would be expected to be considerably smoother when flowing across water than outside the proposed shorelines. None of those profiles shows a flat base over the LA–LD, but all of the upstream margins of the proposed lake positions coincide with steps in the basal topography. In some cases, our radar did not receive a basal signal near topographical steps. On the other hand, the radar observed remarkably large height differences over short distances. In summary, this does not support the hypothesis of lakes as major driver for the genesis of Recovery ice stream.

Still, we lack a considerable amount of ice thickness data within the main trunk of the ice stream upstream of lakes R5R8. In this area, the ice stream is, however, already established and thus we think that it does not limit our analysis of the cause of ice stream genesis. Fortunately, Forsberg et al. (2018) have considerably increased the database in this area so that now both data sets together form a useful basis for modeling studies.

5. Conclusion

Within this study, we tested the hypothesis of large lakes to be present at the base of Recovery Glacier, as well as the possibility of these lakes to be dynamic and governing ice stream genesis.

We have to conclude that with the radar system used, we were unable to determine the basal reflection coefficient with sufficient accuracy to distinguish reliably between wet, dry, and swampy areas. In addition to the specific characteristics of our radar system, there is also a general limit for a reliable estimate of the basal reflection coefficient due to the high uncertainty of the absorption rate in ice. The uncertainty in the estimation of the temperature profile and the limited knowledge of impurities are both factors that could generally become critical to this approach if the transmitted power is insufficient to allow the signal to be well above the noise level. The loss of radar returns we observed is consistent with warm ice found in some areas of Recovery Glacier. This highlights the importance of ice sheet modeling and also the urgent need for improved geothermal heat flux estimates. However, while new radar systems, such as CReSIS MCorRDS or AWI's new ultrawideband radar, can improve the detection of basal reflections, the uncertainties in estimating the rate of absorption of radar waves in ice will continue to be a strong limitation for a reliable estimate of the basal reflection coefficient. Here forward modeling may help to assess the limitations of different systems and to understand the effect of variability in thickness of water bodies over short distances on basal return power.

Our analysis strengthens the hypothesis that the features LA–LD are topographically controlled features rather than lakes. A wet base downstream in the main trunk would be consistent with our findings regarding the reflection coefficient, ice, and hydrology modeling. Two locations where prominent surface elevation change was found in altimetry in this and previous studies are covered well with radar data and basal returns. Also, there the existence of a lake cannot be confirmed despite the existence of a solid database. This raises doubts about the surface elevation change approach to be applicable for subglacial lake detection. It also implies limits on the ability to observe subglacial lake drainage based on satellite altimetry and shines new light on the dynamics of subglacial lakes. Our study emphasizes the grand challenges presented by Ashmore and Bingham (2014) that technological improvements are essential.

References

Arthern, R. J., Winebrenner, D. P., & Vaughan, D. G. (2006). Antarctic snow accumulation mapped using polarization of 4.3-cm wavelength microwave emission. *Journal of Geophysical Research*, 111, D06107. https://doi.org/10.1029/2004JD005667

Ashmore, D. W., & Bingham, R. G. (2014). Antarctic subglacial hydrology: Current knowledge and future challenges. *Antarctic Science*, 26(6), 758–773. https://doi.org/10.1017/S0954102014000546

Ashmore, D. W., Bingham, R. G., Hindmarsh, R. C. A., Corr, H. F. J., & Joughin, R. I. (2014). The relationship between sticky spots and radar reflectivity beneath an active West Antarctic ice stream. *Annals of Glaciology*, 55(67), 29–38. https://doi.org/10.3189/2014AoG67A052

Barnes, R., Lehman, C., & Mulla, D. (2014a). An efficient assignment of drainage direction over flat surfaces in raster digital elevation models. *Computers & Geosciences*, 62, 128–135. https://doi.org/10.1016/j.cageo.2013.01.009

Barnes, R., Lehman, C., & Mulla, D. (2014b). Priority-flood: An optimal depression-filling and watershed-labeling algorithm for digital elevation models. *Computers & Geosciences*, 62, 117–127. https://doi.org/10.1016/j.cageo.2013.04.024

Bell, R. E., Studinger, M., Shuman, C. A., Fahnestock, M. A., & Joughin, I. (2007). Large subglacial lakes in East Antarctica at the onset of fast-flowing ice streams. *Nature*, 445, 904–907. https://doi.org/10.1038/nature05554

Bindschadler, R. A., Nowicki, S., Abe-Ouchi, A., Aschwanden, A., Choi, H., Fastook, J., et al. (2013). Ice-sheet model sensitivities to environmental forcing and their use in projecting future sea level (the SeaRISE project). *Journal of Glaciology*, 59(214), 195–224. https://doi.org/10.3189/2013JoG12J125

Bogorodsky, V. V., Bentley, C. R., & Gudmandsen, P. E. (1985). *Radioglaciology*. Dordrecht, Holland: D. Reidel Publishing Company.

British Antarctic Survey (2004). *Antarctic Digital Database* (4th ed.). Cambridge, UK: Scientific Committee on Antarctic Research.

Bueler, E., & Brown, J. (2009). Shallow shelf approximation as a "sliding law" in a thermomechanically coupled ice sheet model. *Journal of Geophysical Research*, 114, F03008. https://doi.org/10.1029/2008JF001179

Carter, S. P., Blankenship, D. D., Peters, M. E., Young, D. A., Holt, J. W., & Morse, D. L. (2007). Radar-based subglacial lake classification in Antarctica. *Geochemistry, Geophysics, Geosystems (G3)*, 8, 1–20. https://doi.org/10.1029/2006GC001408

Christianson, K., Jacobel, W. R., Horgan, H. J., Anandakrishnan, S., & Alley, B. R. (2012). Subglacial Lake Whillans—Ice-penetrating radar and GPS observations of a shallow active reservoir beneath a West Antarctic ice stream. *Earth and Planetary Science Letters*, 331-332, 237–245. https://doi.org/10.1016/j.epsl.2012.03.013

Comiso, J. C. (2000). Variability and trends in Antarctic surface temperatures from in situ and satellite infrared measurements. *Journal of Climate*, 13(10), 1674–1696. https://doi.org/10.1175/1520-0442(2000)013h1674:VATIASi2.0.CO;2

Davis, J. L., & Annan, A. P. (1989). Ground-penetrating radar for high-frequency mapping of soil and rock stratigraphy. *Geophysical Prospecting*, 37, 531–551.

Diez, A., Matsuoka, K., Ferraccioli, F., Jordan, T. A., Corr, H. F. J., Kohler, J., et al. (2018). Basal settings control fast ice flow in the Recovery/Slessor/Bailey Region, East Antarctica. *Geophysical Research Letters*, 45, 2706–2715. https://doi.org/10.1002/2017GL076601

Feldmann, J., Albrecht, T., Khroulev, C., Pattyn, F., & Levermann, A. (2014). Resolution-dependent performance of grounding line motion in a shallow model compared to a full-stokes model according to the MISMIP3d intercomparison. *Journal of Glaciology*, 60(220), 353–360. https://doi.org/10.3189/2014JoG13J093

Floricioiu, D., Jaber, W. A., & Jezek, K. (2014) TerraSAR-X and TanDEM-X observations of the Recovery Glacier system, Antarctica. In *2014 IEEE Geoscience and Remote Sensing Symposium* (pp. 4852–4855). Quebec City, QC: IEEE. https://doi.org/10.1109/IGARSS.2014.6947581

Forsberg, R., Olesen, A. V., Ferraccioli, F., Jordan, T. A., Matsuoka, K., Zakrajsek, A., et al. (2018). Exploring the Recovery Lakes region and interior Dronning Maud Land, East Antarctica, with airborne gravity, magnetic and radar measurements. *Geological Society, London, Special Publications*, *461*(1), 23–34. https://doi.org/10.1144/SP461.17

Fortuin, J. P. F., & Oerlemans, J. (1990). The parameterization of the annual surface temperature and mass balance of Antarctica. *Annals of Glaciology*, *14*, 78–84. https://doi.org/10.3189/S0260305500008302

Fox Maule, C., Purucker, M. E., Olsen, N., & Mosegaard, K. (2005). Heat flux anomalies in Antarctica revealed by satellite magnetic data. *Science*, *309*(5733), 464–467. https://doi.org/10.1126/science.1106888

Fretwell, P., Pritchard, H. D., Vaughan, D. G., Bamber, J. L., Barrand, N. E., Bell, R., et al. (2013). Bedmap2: Improved ice bed, surface and thickness datasets for Antarctica. *The Cryosphere*, *7*(1), 375–393. https://doi.org/1143 10.5194/tc-7-375-2013

Fricker, H. A., Carter, S. P., Bell, R. E., & Scambos, T. (2014). Active lakes of Recovery Ice Stream, East Antarctica: A bedrock-controlled subglacial hydrological system. *Journal of Glaciology*, *60*(223), 1015–1030. https://doi.org/10.3189/2014JoG14J063

Gades, A. M., Raymond, C. F., Conway, H., & Jacobel, R. W. (2000). Bed properties of Siple Dome and adjacent ice streams, West Antarctica, inferred from radio-echo sounding measurements. *Journal of Glaciology*, *46*(152), 88–94. https://doi.org/10.3189/172756500781833467

Golledge, N. R., Levy, R. H., McKay, R. M., & Naish, T. R. (2017). East Antarctic ice sheet most vulnerable to Weddell Sea warming. *Geophysical Research Letters*, *44*, 2343–2351. https://doi.org/10.1002/2016GL072422

Gorman, M. R., & Siegert, M. J. (1999). Penetration of Antarctic subglacial lakes by VHF electromagnetic pulses: Information on the depth and electrical conductivity of basal water bodies. *Journal of Geophysical Research*, *104*(B12), 29,311–29,320. https://doi.org/10.1029/1999JB900271

Gudlaugsson, E., Humbert, A., Kleiner, T., Kohler, J., & Andreassen, K. (2016). The influence of a model subglacial lake on ice dynamics and internal layering. *The Cryosphere*, *10*(2), 751–760. https://doi.org/10.5194/tc-10-751-2016

Helm, V., Humbert, A., & Miller, H. (2014). Elevation and elevation change of Greenland and Antarctica derived from CryoSat-2. *The Cryosphere*, *8*(4), 1539–1559. https://doi.org/10.5194/tc-8-1539-2014

Herron, M. M., & Langway, C. C. Jr. (1980). Firn densification: An empirical model. *Journal of Glaciology*, *25*(93), 373–385. https://doi.org/10.3189/S0022143000015239

Hippel, A. (Ed.) (1958). *Dielectric Materials and Applications* (2nd ed.). New York: The Technology Press of M.I.T. Cambridge, Massachusetts, and John Wiley & Sons, Inc. New York.

Jacobel, R. W., Lapo, K. E., Stamp, J. R., Youngblood, B. W., Welch, B. C., & Bamber, J. L. (2010). A comparison of basal reflectivity and ice velocity in East Antarctica. *The Cryosphere*, *4*(4), 447–452. https://doi.org/10.5194/tc-4-447-2010

Jezek, K. C. (1999). Glaciological properties of the Antarctic ice sheet from RADARSAT-1 synthetic aperture radar imagery. *Annals of Glaciology*, *29*, 286–290. https://doi.org/10.3189/172756499781820969

Langley, K., Kohler, J., Matsuoka, K., Sinisalo, A., Scambos, T. A., Neumann, T., et al. (2011). Recovery lakes, East Antarctica, radar assessment of sub-glacial water extent. *Geophysical Research Letters*, *38*, L05501. https://doi.org/10.1029/2010GL046094

Langley, K., Tinto, K., Block, A., Bell, R., Kohler, J., & Scambos, T. (2014). Onset of fast ice flow in Recovery Ice Stream, East Antarctica: A comparison of potential causes. *Journal of Glaciology*, *60*(223), 1007–1014. https://doi.org/10.3189/2014JoG14J067

Le Brocq, A. M., Hubbard, A., Bentley, M. J., & Bamber, J. L. (2008). Subglacial topography inferred from ice surface terrain analysis reveals a large un-surveyed basin below sea level in East Antarctica. *Geophysical Research Letters*, *35*, L16503. https://doi.org/10.1029/2008GL034728

Le Brocq, A. M., Payne, A. J., & Siegert, M. J. (2006). West Antarctic balance calculations: Impact of flux-routing algorithm, smoothing algorithm and topography. *Computers & Geosciences*, *32*(10), 1780–1795. https://doi.org/10.1016/j.cageo.2006.05.003

Le Brocq, A. M., Payne, A. J., Siegert, M. J., & Alley, R. B. (2009). A subglacial water-flow model for West Antarctica. *Journal of Glaciology*, *55*(193), 879–888. https://doi.org/10.3189/002214309790152564

Leuschen, C., Gogineni, P., Rodriguez-Morales, F., Paden, J., & Allen, C. (2010, updated 2017). IceBridge MCoRDS L2 ice thickness (Antarctica 2011/12, 2012/13) (Tech. Rep.). Boulder, Colorado USA: Boulder, Colorado USA: NASA National Snow and Ice Data Center Distributed Active Archive Center. https://doi.org/10.5067/GDQ0CUCVTE2Q

Leysinger Vieli, G. J.-M. C., Hindmarsh, R. C. A., & Siegert, M. J. (2007). Three-dimensional flow influences on radar layer stratigraphy. *Annals of Glaciology*, *46*, 22–28. https://doi.org/10.3189/172756407782871729

Leysinger Vieli, G. J.-M. C., Hindmarsh, R. C. A., Siegert, M. J., & Sun, B. (2011). Time-dependence of the spatial pattern of accumulation rate in East Antarctica deduced from isochronic radar layers using a 3-D numerical ice flow model. *Journal of Geophysical Research*, *116*, F02018. https://doi.org/10.1029/2010JF001785

Lister, H., & Pratt, G. (1959). Geophysical investigations of the commonwealth trans-Antarctic expedition. *The Geographical Journal*, *125*(3/4), 343–354. https://doi.org/10.2307/1791117

Livingstone, S. J., Clark, C. D., Woodward, J., & Kingslake, J. (2013). Potential subglacial lakes and meltwater drainage pathways beneath the Antarctic and Greenland ice sheets. *The Cryosphere*, *7*, 1721–1740. https://doi.org/10.5194/tcd-7-1177-2013

MacGregor, J. A., Winebrenner, D. P., Conway, H., Matsuoka, K., Mayewski, P. A., & Clow, G. D. (2007). Modeling englacial radar attenuation at Siple Dome, West Antarctica, using ice chemistry and temperature data. *Journal of Geophysical Research*, *112*, F03008. https://doi.org/10.1029/2006JF000717

Matsuoka, K., MacGregor, J. A., & Pattyn, F. (2012). Predicting radar attenuation within the Antarctic ice sheet. *Earth and Planetary Science Letters*, *359-360*, 173–183. https://doi.org/10.1016/j.epsl.2012.10.018

Matsuoka, K., Morse, D., & Raymond, C. F. (2010). Estimating englacial radar attenuation using depth profiles of the returned power, central West Antarctica. *Journal of Geophysical Research*, *115*, F02012. https://doi.org/10.1029/2009JF001496

Nixdorf, U., Steinhage, D., Meyer, U., Hempel, L., Jenett, M., Wachs, P., & Miller, H. (1999). The newly developed airborne RES-system of the AWI as a glaciological tool. *Annals of Glaciology*, *29*, 231–238. https://doi.org/1230 10.3189/172756499781821346

Nowicki, S., Bindschadler, R. A., Abe-Ouchi, A., Aschwanden, A., Bueler, E., Choi, H., et al. (2013). Insights into spatial sensitivities of ice mass response to environmental change from the SeaRISE ice sheet modeling project I: Antarctica. *Journal of Geophysical Research: Earth Surface*, *118*, 1002–1024. https://doi.org/10.1002/jgrf.20081

Oswald, G. K. A., & Gogineni, S. P. (2008). Recovery of subglacial water extent from Greenland radar survey data. *Journal of Glaciology*, *54*(184), 94–106. https://doi.org/10.3189/002214308784409107

Pattyn, F. (2010). Antarctic subglacial conditions inferred from a hybrid ice sheet/ice stream model. *Earth and Planetary Science Letters*, *295*(3-4), 451–461. https://doi.org/10.1016/j.epsl.2010.04.025

Paxman, G. J. G., Jamieson, S. S. R., Ferraccioli, F., Bentley, M. J., Forsberg, R., Ross, N., et al. (2017). Uplift and tilting of the Shackleton Range in East Antarctica driven by glacial erosion and normal faulting. *Journal of Geophysical Research: Solid Earth*, *122*, 2390–2408. https://doi.org/1246 10.1002/2016JB013841

Peters, M. E., Blankenship, D. D., & Morse, D. L. (2005). Analysis techniques for coherent airborne radar sounding: Application to West Antarctic ice streams. *Journal of Geophysical Research*, *110*, B06303. https://doi.org/10.1029/2004JB003222

Purucker, M. (2012). https://websrv.cs.umt.edu/isis/index.php/Antarctica_Basal_Heat_Flux

Rignot, E., Bamber, J. L., van den Boroeke, M. R., Davis, C., Li, Y., van de Berg, W. J., & van Meijgaard, E. (2008). Recent Antarctic ice mass loss from radar interferometry and regional climate modelling. *Nature Geoscience*, *1*, 106–110. https://doi.org/10.1038/ngeo102

Rignot, E., Mouginot, J., & Scheuchl, B. (2011). Ice flow of the Antarctic ice sheet. *Science*, *333*(6048), 1427–1430. https://doi.org/10.1126/science.1208336

Rippin, D., Bamber, J. L., Siegert, M. J., Vaughan, D. G., & Corr, H. F. J. (2006). Basal conditions beneath enhanced-flow tributaries of Slessor Glacier, East Antarctica. *Journal of Glaciology*, *52*(179), 481–490. https://doi.org/10.3189/172756506781828467

Robin, G., Evans, S., & Bailey, J. T. (1969). Interpretation of radio echo sounding in polar ice sheets. *Philosophical Transactions of the Royal Society London Series A*, *265*, 437–505. https://doi.org/10.1098/rsta.1969.0063

Shapiro, N. M., & Ritzwoller, M. H. (2004). Inferring surface heat flux distributions guided by a global seismic model: Particular application to Antarctica. *Earth and Planetary Science Letters*, *223*, 213–224. https://doi.org/10.1016/j.epsl.2004.04.011

Shreve, R. L. (1972). Movement of water in glaciers. *Journal of Glaciology*, *11*, 205–214. https://doi.org/10.3189/S002214300002219X

Siegert, M. J., & Bamber, J. L. (2000). Subglacial water at the heads of Antarctic ice-stream tributaries. *Journal of Glaciology*, *46*(155), 702–703. https://doi.org/10.3189/172756500781832783

Siegert, M. J., & Ridley, J. K. (1998). Determining basal ice-sheet conditions in the Dome C region of East Antarctica using satellite radar altimetry and airborne radio-echo sounding. *Journal of Glaciology*, *44*(146), 1–8. https://doi.org/10.3189/S002214300000229X

Siegert, M. J., Ross, N., Corr, H. F. J., Smith, B., Jordan, T., Bingham, R. G., et al. (2014). Boundary conditions of an active West Antarctic subglacial lake: Implications for storage of water beneath the ice sheet. *The Cryosphere*, *8*(1), 15–24. https://doi.org/10.5194/tc-8-15-2014

Siegert, M. J., Ross, N., & Le Brocq, A. M. (2016). Recent advances in understanding antarctic subglacial lakes and hydrology. *Philosophical Transactions of the Royal Society A: Mathematical, Physical and Engineering Sciences*, *374*(2059), 20140306. https://doi.org/10.1098/rsta.2014.0306

Siegert, M. J., Ross, N., Li, J., Schroeder, D. M., Rippin, D., Ashmore, D., et al. (2016). Subglacial controls on the flow of Institute Ice Stream, West Antarctica. *Annals of Glaciology*, *57*(73), 19–24. https://doi.org/10.1017/aog.2016.17

Smith, B. E., Fricker, H. A., Joughin, I. R., & Tulaczyk, S. (2009). An inventory of active subglacial lakes in antarctica detected by ICESat (2003–2008). *Journal of Glaciology*, *55*(192), 573–595. https://doi.org/10.3189/002214309789470879

Smith, W., & Wessel, P. (1990). Gridding with continuous curvature splines in tension. *Geophysics*, *55*(3), 293–305.

Vallelonga, P., Christianson, K., Alley, R. B., Anandakrishnan, S., Christian, J. E. M., Dahl-Jensen, D., et al. (2014). Initial results from geophysical surveys and shallow coring of the Northeast Greenland Ice Stream (NEGIS). *The Cryosphere*, *8*(4), 1275–1287. https://doi.org/10.5194/tc-8-1275-2014

van Wessem, J. M., Reijmer, C. H., Morlighem, M., Mouginot, J., Rignot, E., Medley, B., et al. (2014). Improved representation of East Antarctic surface mass balance in a regional atmospheric climate model. *Journal of Glaciology*, *60*(222), 761–770. https://doi.org/10.3189/2014JoG14J051

van de Berg, W. J., van den Broeke, M. R., Reijmer, C. H., & van Meijgaard, E. (2006). Reassessment of the Antarctic surface mass balance using calibrated output of a regional atmospheric climate model. *Journal of Geophysical Research*, *111*, D11104. https://doi.org/10.1029/2005JD006495

Weikusat, I., Jansen, D., Binder, T., Eichler, J., Faria, S. H., Wilhelms, F., et al. (2017). Physical analysis of an Antarctic ice core—Towards an integration of micro- and macrodynamics of polar ice. *Philosophical Transactions of the Royal Society of London A: Mathematical, Physical and Engineering Sciences*, *375*(2086), 20150347. https://doi.org/10.1098/rsta.2015.0347

Winkelmann, R., Martin, M. A., Haseloff, M., Albrecht, T., Bueler, E., Khroulev, C., & Levermann, A. (2011). The Potsdam parallel ice sheet model (PISM-PIK)— Part 1: Model description. *The Cryosphere*, *5*(3), 715–726. https://doi.org/10.5194/tc-5-715-2011

Wright, A. P., Young, D. A., Bamber, J. L., Dowdeswell, J. A., Payne, A. J., Blankenship, D. D., & Siegert, M. J. (2014). Subglacial hydrological connectivity within the Byrd Glacier catchment, East Antarctica. *Journal of Glaciology*, *60*(220), 345–352. https://doi.org/10.3189/2014JoG13J014

Wright, A. P., Young, D. A., Roberts, J. L., Schroederm, D. M., Bamberm, J. L., Dowdeswell, J. A., et al. (2012). Evidence of a hydrological connection between the ice divide and ice sheet margin in the Aurora Subglacial Basin, East Antarctica. *Journal of Geophysical Research*, *117*, F01033. https://doi.org/10.1029/2011JF002066

Zirizzotti, A., Cafarella, L., Baskaradas, J. A., Tabacco, I. E., Urbini, S., Mangialetti, M., & Bianchi, C. (2010). Dry-wet bedrock interface detection by radio echo sounding measurements. *IEEE Transactions on Geoscience and Remote Sensing*, *48*(5), 2343–2348. https://doi.org/10.1109/TGRS.2009.2038900